Chemical Geology 596 (2022) 120790

Contents lists available at ScienceDirect

Chemical Geology

journal homepage: www.elsevier.com/locate/chemgeo

High helium reservoirs in the Four Corners area of the Colorado Plateau, USA

D.T. Halford [a,*], R. Karolytė [a], P.H. Barry [b], C.J. Whyte [c], T.H. Darrah [c], J.J. Cuzella [d], S. A. Sonnenberg [e], C.J. Ballentine [a]

[a] University of Oxford, Oxford, England, UK
[b] Woods Hole Oceanographic Institution, Woods Hole, MA, USA
[c] The Ohio State University, Columbus, OH, USA
[d] Division of Energy and Mineral Development, Indian Energy and Economic Development, Bureau of Indian Affairs, Lakewood, CO, USA
[e] Colorado School of Mines, Golden, CO, USA

ARTICLE INFO

Editor: Dr Don Porcelli

Keywords:
Helium
Nitrogen
Noble gases
Groundwater
Hydrocarbons
Oil

ABSTRACT

Radiogenic ^{4}He is naturally produced in Earth's crust due to alpha decay of Uranium (U) and Thorium (Th). Helium has unique thermodynamic properties required for the medical imaging industry, aerospace and other fields of high-tech manufacturing, and currently is in increasingly high demand. Despite its economic value, the mechanisms of helium migration and retention in sedimentary basins remain poorly understood.

Oil and gas fields with economic helium (>0.3%) concentrations have been discovered in Paleozoic intervals in the Colorado Plateau, southwestern USA. Here we report new noble gas isotope and abundance data for gas samples (n = 31), from actively producing Paleozoic formations within five fields: Ratherford, Tocito Dome, Navajo Springs, Pinta Dome, and Dineh-Bi-Keyah. Helium concentrations range from 0.01% to 7.9% with varying amounts of liquid and gaseous hydrocarbons, N_2, and CO_2. We present multi-stage gas, water, and oil equilibration models to account for the observed noble gas elemental and isotopic signatures. Oil-dominated systems are explained by a closed system oil/water equilibration and subsequent admixture of air. He-rich dry gas samples exhibit uniform $^{4}He/N_2$ ratios consistent with the regional mean values, suggesting a common crustal source and no subsequent fractionation. In contrast, air-derived $^{20}Ne/^{36}Ar$ ratios are highly fractionated. These observations are consistent with a tectonically controlled crustal gas release from the basement, groundwater saturation with ^{4}He and N_2, and subsequent degassing. Extensive gas-water interaction (i.e., migration) leads to extreme fractionation of $^{20}Ne/^{36}Ar$, but does not affect $^{4}He/N_2$ due to water saturation with crustal gases released from the basement.

We show the volume of rock required to have produced helium in the reservoir to be significantly larger than the current reservoir volume immediately beneath the field. Therefore, the reservoir helium concentration cannot be sourced by in-reservoir decay of U and Th and instead requires a process to incorporate exogenous sources of helium in the reservoir without significant dilution from hydrocarbons. For helium-rich fields, excess helium is sourced from the Precambrian granitic basement likely utilizing a large area beneath the field area (i.e., crustal gas mobilization and transport via fracture zones), consistent with the degree of water contact. Deep crustal faults in the Precambrian basement are in close proximity to the high helium fields, indicating that these structures are potentially serving as primary migration conduits via advective fluid flow.

1. Introduction

Helium (He) is the second lightest element and the lightest noble gas in the observable universe. It has two stable isotopic forms: ^{3}He (primordial) and ^{4}He (radiogenic decay). Although helium is the second most abundant element in the galaxy, it is relatively rare on Earth. Despite helium's rarity on Earth, people have managed to extract it from the ground, typically when it co-occurs with natural gas, and have developed various advanced applications due to its stable electron configuration and low atomic mass (Chan, 2013). Applications of helium

* Corresponding author.
E-mail address: daniel.halford@earth.ox.ac.uk (D.T. Halford).

https://doi.org/10.1016/j.chemgeo.2022.120790
Received 9 July 2021; Received in revised form 15 December 2021; Accepted 24 February 2022
Available online 5 March 2022

include: Magnetic Resonance Imaging (MRIs), spectrometry, chromatography, dirigible/lifting, electronics, semiconductors, science/engineering, fiber optics, diving, welding, and controlled atmospheres (National Research Council, 2010).

Helium reservoirs, which have been traditionally discovered serendipitously as a by-product of hydrocarbon exploration, can be classified by their major gas component: N_2, CH_4, and CO_2-rich. After the Kansas, USA initial discovery, additional helium discoveries have been made across the USA in Texas, Oklahoma, Wyoming, Kansas, New Mexico, Arizona, Utah, Colorado, and Montana (USGS, 2000-2021). Fields within the Four Corners area (New Mexico and Arizona) contain helium up to ~10% (Brennan et al., 2016) (Fig. 1). The economic threshold for a helium-rich field is 0.3% for primary (standalone) and secondary (with other hydrocarbons) production, and 0.04% from the production of liquefied natural gas (National Research Council, 2010; Brennan et al., 2016; Halford, 2018; Anderson, 2018; Boreham et al., 2018). When the terms economic or non-economic helium are used in this study they are referring strictly to the molar percentage of helium found in the gas stream and do not refer to reservoir volume, producibility, feasibility, and/or the economics of various separation strategies (e.g., pressure swing adsorption, nitrogen rejection). Despite helium not being recognized as a valuable primary resource historically (i.e., often vented to the atmosphere because helium is not combustible), currently helium is being considered as a primary exploration target due to favorable economics and increasing global demand.

To aid in the exploration of helium, helium system models, which are a slight variation to the original petroleum system models, are being developed by utilizing elemental compositions and isotopes of noble gases, hydrocarbons, and non-hydrocarbons (Magoon and Dow, 1994a, 1994b; Halford, 2018; Flude et al., 2019). Considering helium as a primary exploration target, there are previously reported critical requirements for the discovery of an economic helium play in the Four Corners area: 1) a portion of shallow crust (basement) to supply helium (source rock), 2) long stable periods to allow helium to accumulate within the impermeable source rocks, 3) faulting/igneous activity/other younger tectonic events, which aided in the advection of helium from the source rock (primary migration) into the overlying sedimentary strata, 4) gas – water interactions with large volumes of pore water (secondary/lateral migration), 5) the presence of a separate migration gas phase to exsolve the helium from solution into a trap, 6) lack of large basin scale charging events of hydrocarbons, which might dilute the helium in the reservoir (edges of a petroleum system are favorable), 7) the presence of structural, stratigraphic, or combination structural-stratigraphic traps, 8) a seal with very tight and impermeable lithology (evaporites, tight mudstones, tight carbonates, or igneous intrusions), and 9) a period of relative quiescence without large-scale tectonic events to protect the seal and allow additional helium accumulation (Ballentine and Burnard, 2002; Ballentine and Sherwood-Lollar, 2002; Broadhead and Gillard, 2004; Brown, 2010; Danabalan, 2017, Danabalan et al., 2022; Halford, 2018; Zhang et al., 2019)

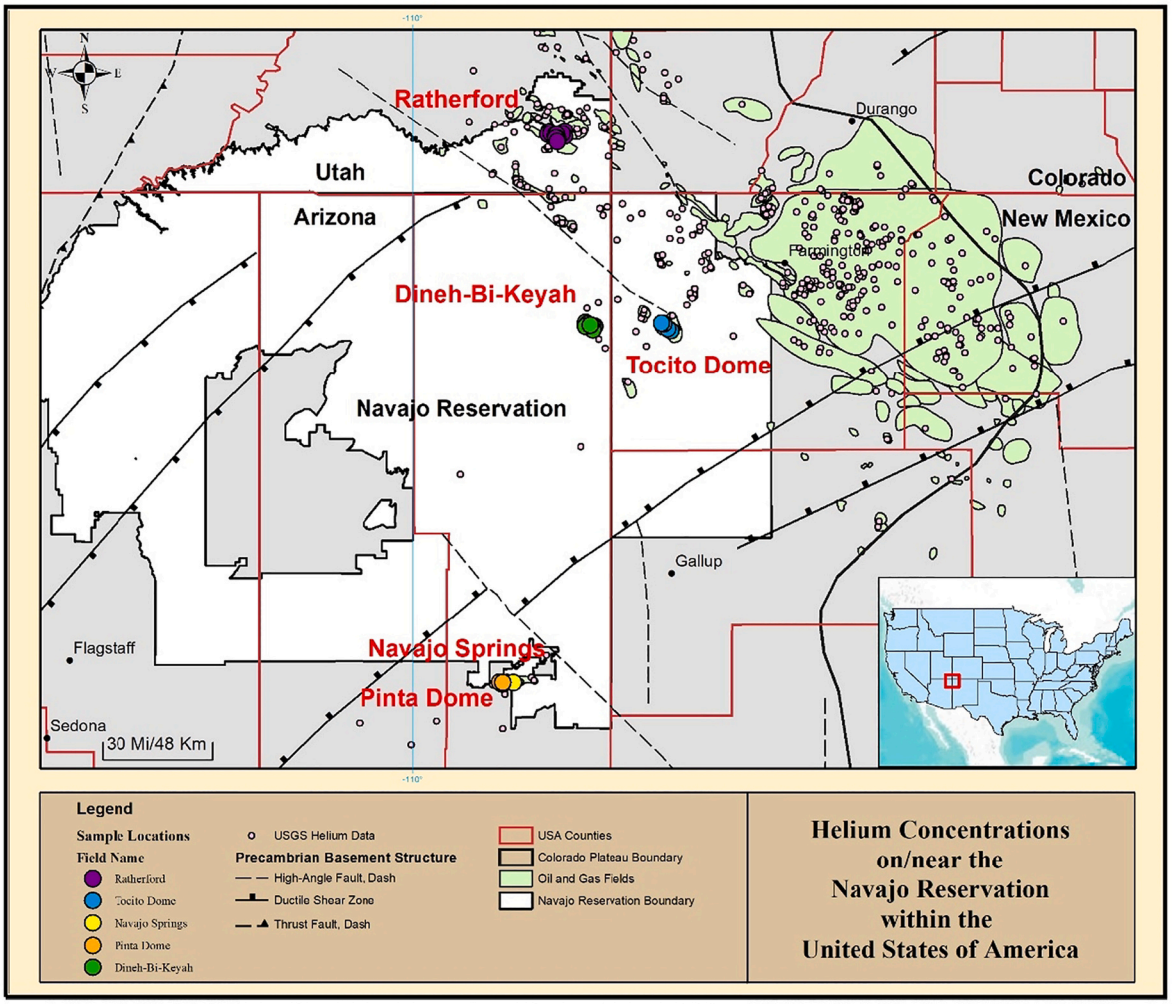

Fig. 1. Distribution of helium from historical Four Corners area wells along with current sampled locations, which are shown by large colored circles (USGS helium data - Brennan et al., 2016). Solid fault lines are based on geologic data, while dashed lines are based on geophysical data (Precambrian basement faults - Craddock et al., 2017; Sims et al., 2008).

(Table A.1, Fig. A.1). This study will investigate several of these factors (1–6) to explain the helium occurrences and lay out a more accurate definition of the helium system in the Four Corners area, which ultimately serves to increase the viability of helium exploration models, lower exploration risk, and spur economic development.

2. Geologic background

2.1. Regional tectonic history of the Colorado Plateau

The Colorado Plateau, which is an elevated crustal block of relatively undeformed strata, straddles Colorado, Utah, New Mexico, and Arizona and is bounded by the Basin and Range province to the northwest, the Rocky Mountains to the northeast, the Rio Grande Rift to the southeast, and the Mogollon Rim to the southwest (Foos, 1999; Gilfillan et al., 2008). The Colorado Plateau is composed of generally flat to slightly dipping sedimentary rocks, which uncomfortably overlie metamorphic and igneous Paleoproterozoic basement rocks (Condie, 1986; Tingey et al., 1991; Re, 2017). The Mazatzal and Yavapai accretionary terranes make up the Paleoproterozoic basement (Karlstrom and Bowring, 1988). There are no structural mountain ranges on the plateau, only volcanic mountains. Volcanism is present around the peripherals of the plateau with minor occurrences within the plateau's boundaries, most likely influencing the low heat flow of the plateau (Gilbert et al., 2007). Although relatively undeformed (possibly due to a thick crust), zones of weakness in basement rocks have localized deformation (i.e., folds and faults, and concomitant fracture systems), which may influence gas migration paths.

The first stage of tectonic uplift commenced during the late Cretaceous (80–50 Ma) was related to Sevier and Laramide contractile deformation (Huntoon., 1974; Roy, 2005; Roberts et al., 2012). During Late Eocene to Miocene times (35–15 Ma) there was a second phase of uplift (Roberts et al., 2012). It is proposed that Cenozoic uplift was influenced by the flat slab subduction and demise of the Farallon oceanic plate (i.e., Farallon rollback) (Hernández-Uribe and Palin, 2019). This caused the delamination of the mantle lithosphere underneath the plateau, which was replaced by rising asthenosphere (Levander et al., 2011; Hernández-Uribe and Palin, 2019). During the Oligocene, magmas were introduced into the sedimentary sections through deep-seated faults resulting in laccoliths of intermediate composition (Foos, 1999; Fitton et al., 1991; Gilfillan et al., 2008; Roberts et al., 2012; Re, 2017). Around 5 Ma ago, the Colorado Plateau experienced epeirogenic uplift associated with regional extensional tectonism (Baars, 2000; Roy, 2005). According to Foos (1999), this uplift was facilitated by tilting of the plateau to the north and by the reactivation of preexisting faults.

2.2. Generalized stratigraphy

The stratigraphy of the Colorado Plateau consists of Proterozoic through Cenozoic aged sediments (Fig. A.2) with most sedimentary rocks being deposited in a passive margin (i.e., coastal terrestrial or shallow marine origin) (Trexler, 2014). On the plateau, episodes of volcanism contributed to the lithologic record from Paleogene - Quaternary. Within the Colorado Plateau's stratigraphic record, Paleozoic rocks in the Four Corners area produced high He concentrations (Rauzi, 2003; Broadhead and Gillard, 2004; Brown, 2010; Halford, 2018). Paleozoic rocks with helium potential in the Four Corners region consist of Devonian, Mississippian, Pennsylvanian, and Permian units. The Devonian section includes carbonates (limestones, dolomites), glauconitic sandstones, and black shales. The Mississippian section is predominately limestones. Carbonates (limestones), sandstones, and black shales comprise the Pennsylvanian, whereas the Permian section is mostly sandstones (Fassett, 2010). Oligocene sills within Pennsylvanian strata have produced helium in the Dineh-Ki-Keyah Field in the Four Corners area (McKenny and Masters, 1968; Masters, 2000; Rauzi, 2015; Halford, 2018). In this study, gas samples were obtained from the McCracken Sandstone (Dineh-Bi-Keyah Field), the Barker Creek (Dineh-Bi-Keyah and Tocito Dome fields), a sill intruding the Barker Creek (Dineh-Bi-Keyah Field), the Desert Creek (Ratherford Field), and the Coconino Sandstone (Navajo Springs and Pinta Dome fields).

3. Methods

3.1. Sample collection

Natural gas was sampled from existing wellheads on and near the Navajo Nation, from helium producing Paleozoic formations. Duplicate gas samples were collected in the field from 31 actively producing wells from Utah, New Mexico, and Arizona with stainless-steel cylinders (non-noble gases) and copper tubes (noble gases). The cylinders were evacuated and pre-baked stainless-steel cylinders and thick-walled refrigerator grade copper tubes, which are 40.6 cm (15.98 in) long, and have a 0.95 cm (0.374 in) outside diameter. The cylinders were fitted with vacuum modified Swagelok valves. Copper tubing was connected to the in-line system, allowing for the simultaneous collection of stainless steel and copper tubes. To minimize contamination, once the stainless-steel cylinders and copper tubes were connected in-line to the producing well, they were purged for approximately 10 min each (greater than 50 tube volumes of gas) to negate air contamination (Darrah et al., 2015; Kang et al., 2016). Once the samples were successfully collected, the stainless-steel cylinders were sealed using vacuum in-line modified valves while the copper tubes were sealed with brass refrigeration clamps with a 0.762 mm gap (Darrah et al., 2013; Darrah et al., 2015; Kang et al., 2016).

3.2. Laboratory analyses

The laboratory analyses were divided into: noble gas (elemental and isotopic abundance), major gas components, stable isotopes of carbon, and stable isotopic values of nitrogen.

For the noble gas analyses a Thermo Fisher Helix Split Flight Tube (SFT) Noble Gas mass spectrometer was utilized at the Ohio State University Noble Gas Laboratory (OSU NGL). Darrah and Poreda (2012) cover the noble gas procedures for the purification and analyses of gas samples. The average precision for noble gas concentrations based on standard reproducibility for noble gas isotope concentrations are as follows: ^{4}He (0.69%), ^{22}Ne (1.09%), ^{36}Ar (0.31%), ^{84}Kr (1.51%), and ^{130}Xe (1.58%).

To measure the major gas components (hydrocarbon and non-hydrocarbon compositions), an SRS Quadrupole mass spectrometer and the SRI 8610C Multi-Gas 3+ gas chromatograph with a flame ionization detector and thermal conductivity detector were utilized (Hunt et al., 2012; Darrah and Poreda, 2012; Kang et al., 2016). The standard errors were all less than ±2.97% for major gas concentrations. The average results of the external precision analyses are: CH_4 (1.34%), C_2H_6 (1.57%), C_3H_8 (1.44%), C_4H_{10}-i (2.84%), C_4H_{10}-n (2.86%), C_5H_{12}-i (2.97%), C_5H_{12}-n (2.91%), N_2 (0.98%), CO_2 (1.21%), and Ar (0.63%) based on daily replicate measurements during analyses.

Darrah et al. (2013), Jackson et al. (2013), Darrah et al. (2015b), and Harkness et al. (2017), describe the procedures for obtaining stable isotopic values for C in CH_4. For the hydrocarbon isotopic percentages, firstly a Thermo Finnigan Trace Ultra gas chromatograph was used and secondly a Thermo Fisher Delta V Plus with combustion and dual inlet isotope ratio mass spectrometer was utilized. Detection limits are 0.001 cm^3STP/cm^3 for CH_4. The $\delta^{13}C$-CH_4 are calculated versus the Vienna Peedee belemnite (VPDB) with a reproducibility for CH_4 (± 0.1‰). The $\delta^{13}C$-CH_4 values are shown in per mil (‰).

The methods of the stable isotopic analyses of nitrogen (N_2) are described in Darrah et al. (2013), Darrah et al. (2015), Harkness et al. (2017), and Jackson et al. (2013). Using the same methods as described above (Thermo Finnigan Trace Ultra gas chromatographic separation, followed by using the Thermo Fisher Delta V Plus with dual inlet isotope

ratio mass spectrometry), the detection limits of nitrogen isotopes are 0.001 cm^3STP/cm^3 for $\delta^{15}N\text{-}N_2$. The $\delta^{15}N\text{-}N_2$ values (versus air) have a N_2 reproducibility of ±0.3‰.

Utilizing established atmospheric air standards from Lake Erie, Ohio air, several synthetic natural gas standards from Praxair, which include referenced/cross-validated laboratory standards of N_2, CO_2, O_2, C_1-C_5, and the Yellowstone MM standard, average external precisions were determined (Tedesco et al., 2010; Harkness et al., 2017).

4. Results

The bulk major gas concentrations (Table 1, Fig. 2) as well as noble gas abundance and isotope ratios ($n = 31$) are presented in Table 2. Observations regarding the fields are: 1) the Ratherford Field is mostly composed of methane, ethane, and propane, with trace amounts of helium. 2) The Tocito Dome Field has marginally economic levels of helium along with substantial methane contributions. Thus, the Ratherford and Tocito Dome are CH_4-rich fields. 3) The Navajo Springs and Pinta Dome samples have minute amounts of methane, are rich in nitrogen, and have the highest helium concentrations observed in this study. 4) The Dineh-Bi-Keyah (DBK) samples are nitrogen-rich, have high helium and variable CO_2 abundances. Thus, Dineh-Bi-Keyah, Pinta Dome, and Navajo Springs fields are classified as He-rich fields.

4.1. Major volatiles and stable isotopes

We establish the hydrocarbon-rich (CH_4-rich) fields as the Ratherford and Tocito Dome fields, and the helium-rich (He-rich) fields as the Navajo Springs, Pinta Dome, and Dineh-Bi-Keyah fields. The data ranges for N_2 (%) are: 0.7–8.0 (CH_4-rich); 76.6–91.3 (He-rich). $\delta^{15}N$ (N_2) (‰) versus air: −11.7 to −2.5 (CH_4-rich); 3.0 to 7.6 (He-rich). CH_4 (%): 51.8–78.9 (CH_4-rich); 0.02–2.7 (He-rich). $\delta^{13}CH_4$ (‰ VPDB):-53.6 to −43.0 (CH_4-rich); −36.2 to −30.6 (He-rich). ΣC_2+ (%): 12.8–43.4 (CH_4-rich); 0.00003–0.04 (He-rich).

4.2. Noble gases

Bulk helium for the fields are: 0.01–0.6% (CH_4-rich); 5%–8% (He-rich). ^4He ($\mu cm^3/cm^3$): 146.0–6071.3 (CH_4-rich); 50,390.1-79,200.3 (He-rich). The helium isotopic ratios $^3He/^4He$, expressed as R/R_a [$(^3He/^4He)\ R/R_a = (^3He/^4He)_{measured} / (^3He/^4He)_{atmosphere}$)], for the CH_4-rich fields are strongly radiogenic (0.02–0.09 Ra); while the He-rich fields contain a mantle component (0.05–0.22 Ra) (Andrews, 1985; Ballentine and Burnard, 2002) (Fig. 3). Ra values are reported relative to the air value $Ra = 1.384 \times 10^{-6}$ (air = 1 Ra; Clarke et al., 1976; Sano et al., 1988). The data ranges for $^4He/^{20}Ne$ are: 1654.9-178,172.2 (CH_4-rich); 11,260.7-213,865.4 (He-rich). Since the $^4He/^{20}Ne$ ratios are all significantly higher than the ASW value of 0.288 (Kipfer et al., 2002), this indicates that air derived He contributions are negligible.

^{20}Ne ($\mu cm^3/cm^3$) for the fields are: 0.01–0.2 (CH_4-rich); 0.3–5.7 (He-rich). $^{20}Ne/^{22}Ne$: 9.5–9.8 (CH_4-rich); 9.2–9.7 (He-rich). $^{21}Ne/^{22}Ne$: 0.03–0.06 (CH_4-rich); 0.04–0.08 (He-rich). Ratios greater than the air value for $^{21}Ne/^{22}Ne$ (0.029) are attributed to crustal input (Ballentine and O'Nions, 1992).

The data ranges for ^{40}Ar ($\mu cm^3/cm^3$) are: 46.2–1106.4 (CH_4-rich); 4230.1–23,204.8 (He-rich). $^{40}Ar/^{36}Ar$: 355.8–5177.4 (CH_4-rich); 1291.9-17,083.2 (He-rich). Compared to the air $^{40}Ar/^{36}Ar$ value of 298.56, the ratios indicate crustal enrichment (Lee et al., 2006).

The data ranges for ^{84}Kr (ncm^3/cm^3) are: 1.3–48.4 (CH_4-rich); 17.4–120.9 (He-rich). ^{132}Xe (ncm^3/cm^3): 0.04–3.0 (CH_4-rich); 3.3–18.2 (He-rich). Kr ($^{86}Kr/^{84}Kr$) and Xe ($^{132}Xe/^{130}Xe$) isotopic ratios are air like (0.3; $^{86}Kr/^{84}Kr$) and (6.6; $^{132}Xe/^{130}Xe$) (Aregbe et al., 1996; Moreira and Allegre, 1998; Pepin, 2000; Porcelli and Ballentine, 2002; Ballentine and Burnard, 2002; White, 2015).

5. Discussion

5.1. Crustal influence

Noble gases can be utilized to fingerprint natural gases and determine the origin of different gas families (Ballentine et al., 2002; Gilfillan et al., 2008; Gilfillan et al., 2009; Hunt et al., 2012). By utilizing helium isotopes, ^4He concentrations, and $^{40}Ar/^{36}Ar$ values, we are able to clearly distinguish four different source families of gases on Fig. 3A and B and determine their relative origin and mixing between endmembers. Helium production ratios in the continental crust are ~0.02 R/R_a (Andrews, 1985; Ballentine and Burnard, 2002; Boreham et al., 2018), compared with an average subcontinental lithospheric mantle value of 6.1 ± 2.1 R/R_a (Day et al., 2015).

By plotting He isotopes versus $^{40}Ar/^{36}Ar$ (Fig. 3A) and ^4He concentrations (Fig. 3B), we observe that Four Corners gases are derived from a continental crust source with a contribution from the mantle. The Navajo Springs and the Pinta Dome samples have the highest He isotope values, indicating a resolvable mantle contribution relative to crustal sources based on the R/R_a ratios. Air corrected Rc/Ra values are equal to R/Ra values, so air contamination is negligible. In Fig. 3A, increases in radiogenic ^{40}Ar relative to ^{36}Ar in the Dineh-Bi-Keyah samples are observed, possibly associated with a thermal release by a recent igneous activity in the field (Danie, 1978; Masters, 2000). Enrichment in ^{40}Ar tracks with ^4He suggesting a common crustal source.

5.2. Regional nitrogen and noble gas relationships

When plotting $N_2/^{36}Ar$ against $^4He/^{36}Ar$, two groups are observed, the helium-rich and hydrocarbon-rich, which show a regional underlying relationship between radiogenic helium, crustal-sourced N_2, and the groundwater system (Fig. 4). There is a positive correlation between the helium-rich samples of several different fields, which indicates a regional relationship. Helium-rich fields have a consistent regional $^4He/N_2$ ratio of 0.07, while the hydrocarbon-rich Ratherford has a $^4He/N_2$ ratio of 0.018. High-He samples clearly have excess ^4He and N_2 beyond air/groundwater mixing, perhaps due to lack of hydrocarbon dilution. In contrast, radiogenic Ratherford samples exhibit a resolvable portion of air-derived N_2 as well as N_2 from ASW (air-saturated water), suggesting a shallow-sourced water-dominated N_2 component.

Nitrogen isotopes combined with helium (Fig. 5), can be used to delineate N_2 and He sources from organic sedimentary derived nitrogen (i.e., thermal cracking of hydrocarbons/post – mature and mature organics), and crustal nitrogen released from the basement during low temperature metamorphism or from clays (Cartigny and Marty, 2013; Ballentine and Sherwood-Lollar, 2002). In Fig. 5, air, mantle-derived N_2, and mature organics are negligible in high helium samples, suggesting there must be another source contributing to the N_2 (Halford, 2018). Dominant contributions from the post mature organics, clays and metasediments should be discounted for the hydrocarbon–rich samples.

5.2.1. Hydrocarbon-rich fields

The N_2 in Ratherford and Tocito Dome samples are likely from an organic source (Fig. 5) as a minor component of hydrocarbons (Fig. 2). However, Ratherford samples are likely receiving a portion of their N_2 from air as the samples plot close to the air end-member in $^{20}Ne/^{22}Ne$ vs $^{21}Ne/^{22}Ne$ space (Fig. 6), and near the $\delta^{15}N$ (N_2) air value of 0‰ in Fig. 5. Additionally, we hypothesize that there is a ^4He-poor/^{15}N-depleted endmember influencing the Ratherford samples and a ^4He-rich/^{15}N-depleted endmember influencing the Tocito Dome samples in Fig. 5.

Ratherford and Tocito Dome samples fall within the overlapping range of mantle (small but discernible mantle component is evident from He isotopes) and mature organics (−7 to −3‰ $\delta^{15}N$), suggesting a combination of both mantle and mature organics in N isotope space. The most likely scenario is that the negative nitrogen signature is not mantle

Table 1
Elemental gas values, R: Ratherford, TD: Tocito Dome, NS: Navajo Springs, PD: Pinta Dome, & DBK: Dineh-Bi-Keyah. Other abbreviations: below detection limit (b.d.l.) and non-applicable (n/a).

ID	CH_4 cm^3STP/cm^3	± cm^3STP/cm^3	C_2H_6 cm^3STP/cm^3	± cm^3STP/cm^3	C3 cm^3STP/cm^3	± cm^3STP/cm^3	Ci-4 cm^3STP/cm^3	± cm^3STP/cm^3	Cn-4 cm^3STP/cm^3	± cm^3STP/cm^3
R12–23	0.76	9.59E-03	1.27E-01	1.72E-03	4.99E-02	6.69E-04	4.90E-03	1.27E-04	1.37E-02	3.54E-04
R13–41	0.78	9.83E-03	1.27E-01	2.36E-03	4.18E-02	7.11E-04	3.14E-03	8.43E-05	7.67E-03	2.06E-04
R20–66	0.74	9.39E-03	1.49E-01	2.33E-03	5.91E-02	7.09E-04	4.96E-03	1.18E-04	1.25E-02	2.99E-04
R20–42	0.62	7.83E-03	1.77E-01	3.82E-03	1.07E-01	1.43E-03	1.44E-02	3.87E-04	4.16E-02	1.12E-03
R20–44	0.71	8.96E-03	1.55E-01	2.88E-03	6.35E-02	7.56E-04	5.27E-03	1.57E-04	1.30E-02	3.88E-04
R29–31	0.72	9.02E-03	1.56E-01	1.96E-03	6.13E-02	7.60E-04	5.96E-03	1.96E-04	1.25E-02	4.11E-04
R15–33	0.74	9.38E-03	1.34E-01	2.19E-03	4.97E-02	5.52E-04	4.39E-03	1.37E-04	1.09E-02	3.42E-04
R16–41	0.61	7.74E-03	1.95E-01	2.84E-03	1.06E-01	1.32E-03	7.17E-03	2.14E-04	2.09E-02	6.23E-04
R10–14	0.66	8.29E-03	8.72E-02	2.77E-03	3.05E-02	3.26E-04	2.38E-03	6.61E-05	5.95E-03	1.66E-04
R10–32	0.63	7.97E-03	1.72E-01	3.20E-03	9.30E-02	1.14E-03	9.69E-03	2.93E-04	2.95E-02	8.95E-04
R9–34	0.54	6.86E-03	2.21E-01	3.41E-03	1.25E-01	1.68E-03	1.30E-02	3.80E-04	3.43E-02	1.00E-03
R17–13	0.59	7.37E-03	2.11E-01	3.31E-03	1.08E-01	1.25E-03	1.30E-02	3.63E-04	3.64E-02	1.01E-03
R17–11	0.65	8.17E-03	1.93E-01	3.77E-03	9.51E-02	1.02E-03	8.73E-03	2.17E-04	2.51E-02	6.24E-04
R17–22	0.58	7.31E-03	1.76E-01	2.56E-03	1.12E-01	1.56E-03	1.75E-02	5.49E-04	4.72E-02	1.48E-03
R13–12	0.52	5.31E-03	1.72E-01	3.36E-03	1.16E-01	1.71E-03	1.69E-02	4.70E-04	6.12E-02	1.71E-03
TD U 9	0.79	1.05E-02	1.03E-01	1.70E-03	4.11E-02	5.42E-04	6.08E-03	1.57E-04	1.06E-02	2.74E-04
TD U 7	0.78	9.56E-03	9.76E-02	1.82E-03	4.38E-02	5.43E-04	7.46E-03	2.71E-04	1.31E-02	4.75E-04
TD U 12	0.78	1.11E-02	9.51E-02	2.47E-03	3.77E-02	4.75E-04	5.67E-03	1.46E-04	9.50E-03	2.45E-04
TD N 1	0.78	1.27E-02	9.42E-02	2.46E-03	3.85E-02	4.81E-04	5.98E-03	1.30E-04	1.09E-02	2.38E-04
TD N 11	0.78	8.87E-03	9.83E-02	2.67E-03	4.08E-02	5.96E-04	6.40E-03	1.59E-04	1.12E-02	2.79E-04
TD N 6	0.76	9.64E-03	1.06E-01	1.45E-03	3.74E-02	5.34E-04	7.45E-03	1.78E-04	1.33E-02	3.16E-04
NS 31–1	0.01	2.10E-04	1.91E-05	7.94E-07	1.33E-05	7.45E-07	6.91E-06	4.34E-07	1.01E-05	6.37E-07
PD 33–1	0.01	2.92E-04	1.88E-05	9.69E-07	1.85E-05	1.13E-06	9.20E-06	6.70E-07	1.54E-05	1.12E-06
PD 34–1	2.18E-04	5.90E-06	2.96E-07	1.82E-08	b.d.l.	n/a	b.d.l.	n/a	b.d.l.	n/a
DBK B 2	0.02	7.00E-04	1.27E-04	4.00E-06	7.93E-05	3.89E-06	1.63E-05	9.99E-07	2.53E-05	1.55E-06
DBK C 2	0.01	5.34E-04	7.92E-05	4.08E-06	4.53E-05	2.17E-06	8.40E-06	4.81E-07	1.33E-05	7.61E-07
DBK 4	0.01	2.20E-04	6.09E-05	3.42E-06	3.91E-05	1.83E-06	b.d.l.	n/a	b.d.l.	n/a
DBK 24	0.01	3.65E-04	2.98E-05	1.46E-06	1.96E-05	9.97E-07	b.d.l.	n/a	b.d.l.	n/a
DBK 15	0.03	1.16E-03	1.98E-04	6.24E-06	1.21E-04	3.75E-06	2.38E-05	1.41E-06	3.83E-05	2.27E-06
DBK 88 3	0.02	8.32E-04	9.88E-05	4.11E-06	5.20E-05	2.80E-06	1.37E-05	9.23E-07	2.10E-05	1.41E-06
DBK 88 2	2.75E-03	9.41E-05	2.03E-05	1.25E-06	1.24E-05	7.93E-07	b.d.l.	n/a	b.d.l.	n/a

ID	Ci-5 cm^3STP/cm^3	± cm^3STP/cm^3	C-5 cm^3STP/cm^3	± cm^3STP/cm^3	C-6+ cm^3STP/cm^3	± cm^3STP/cm^3	CO_2 cm^3STP/cm^3	± cm^3STP/cm^3	N_2 cm^3STP/cm^3	± cm^3STP/cm^3
R12–23	2.88E-03	8.47E-05	3.34E-03	9.80E-05	1.52E-03	4.85E-05	0.02	2.23E-04	0.02	1.47E-04
R13–41	1.50E-03	4.30E-05	1.75E-03	5.04E-05	7.97E-05	2.55E-06	0.01	1.43E-04	0.02	1.67E-04
R20–66	1.83E-03	5.41E-05	1.93E-03	5.70E-05	5.84E-04	1.87E-05	0.02	2.07E-04	0.01	7.18E-05
R20–42	6.27E-03	1.74E-04	7.83E-03	2.17E-04	5.98E-04	1.91E-05	0.01	8.62E-05	0.01	6.38E-05
R20–44	2.28E-03	8.89E-05	2.65E-03	1.03E-04	1.85E-04	5.92E-06	0.02	2.31E-04	0.02	1.94E-04
R29–31	1.63E-03	5.09E-05	1.63E-03	5.09E-05	b.d.l.	n/a	0.02	1.92E-04	0.01	1.35E-04
R15–33	1.82E-03	5.99E-05	1.89E-03	6.22E-05	7.36E-04	2.36E-05	0.01	1.18E-04	0.04	3.70E-04
R16–41	6.26E-03	2.15E-04	7.60E-03	2.61E-04	2.86E-04	9.16E-06	0.03	3.68E-04	0.01	1.02E-04
R10–14	8.66E-04	2.33E-05	9.31E-04	2.51E-05	2.94E-04	9.41E-06	0.13	2.02E-03	0.08	7.43E-04
R10–32	5.95E-03	1.90E-04	6.44E-03	2.06E-04	8.34E-04	2.67E-05	0.02	3.23E-04	0.02	2.12E-04
R9–34	6.17E-03	1.91E-04	6.28E-03	1.94E-04	5.02E-04	1.61E-05	0.03	3.39E-04	0.01	9.71E-05
R17–13	5.97E-03	2.37E-04	6.91E-03	2.74E-04	2.66E-03	8.51E-05	0.02	3.78E-04	0.01	8.41E-05
R17–11	5.17E-03	1.29E-04	6.94E-03	1.73E-04	5.96E-04	1.91E-05	0.01	5.92E-05	0.01	7.99E-05
R17–22	1.13E-02	3.06E-04	1.16E-02	3.12E-04	7.95E-03	2.54E-04	0.01	1.84E-04	0.02	1.95E-04
R13–12	1.92E-02	6.34E-04	2.82E-02	9.30E-04	2.02E-02	6.45E-04	0.04	5.92E-04	0.01	1.00E-04
TD U 9	3.09E-03	1.08E-04	2.59E-03	9.07E-05	1.52E-03	4.86E-05	0.02	1.86E-04	0.02	2.10E-04
TD U 7	3.49E-03	9.07E-05	3.08E-03	8.00E-05	2.22E-03	7.09E-05	0.02	1.91E-04	0.03	2.51E-04
TD U 12	2.24E-03	7.39E-05	1.87E-03	6.16E-05	9.31E-04	2.98E-05	0.02	2.46E-04	0.04	3.97E-04
TD N 1	2.59E-03	6.48E-05	2.28E-03	5.69E-05	1.11E-03	3.55E-05	0.02	2.11E-04	0.04	3.86E-04
TD N 11	2.88E-03	1.09E-04	2.47E-03	9.36E-05	1.27E-03	4.07E-05	0.02	2.19E-04	0.04	3.03E-04
TD N 6	3.68E-03	1.03E-04	2.85E-03	7.97E-05	2.08E-03	6.65E-05	0.02	2.12E-04	0.05	4.02E-04
NS 31–1	5.57E-06	3.12E-07	5.64E-06	3.16E-07	1.08E-06	3.47E-08	0.01	1.41E-04	0.91	6.29E-03
PD 33–1	1.48E-05	1.03E-06	1.51E-05	1.05E-06	3.03E-06	9.69E-08	0.01	1.10E-04	0.91	4.50E-03
PD 34–1	b.d.l.	n/a	b.d.l.	n/a	b.d.l.	n/a	1.83E-03	3.86E-05	0.90	7.10E-03
DBK B 2	b.d.l.	n/a	b.d.l.	n/a	b.d.l.	n/a	0.13	1.06E-03	0.78	5.02E-03
DBK C 2	b.d.l.	n/a	b.d.l.	n/a	b.d.l.	n/a	0.12	1.07E-03	0.77	4.51E-03
DBK 4	b.d.l.	n/a	b.d.l.	n/a	b.d.l.	n/a	0.14	1.15E-03	0.79	6.00E-03
DBK 24	b.d.l.	n/a	b.d.l.	n/a	b.d.l.	n/a	0.13	9.25E-04	0.78	7.28E-03
DBK 15	b.d.l.	n/a	b.d.l.	n/a	b.d.l.	n/a	0.13	1.33E-03	0.77	4.54E-03
DBK 88 3	b.d.l.	n/a	b.d.l.	n/a	b.d.l.	n/a	0.11	1.04E-03	0.78	3.68E-03
DBK 88 2	b.d.l.	n/a	b.d.l.	n/a	b.d.l.	n/a	0.15	1.85E-03	0.78	3.27E-03

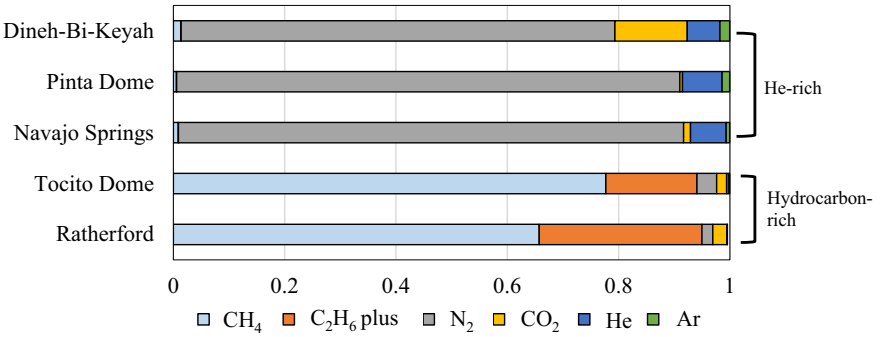

Fig. 2. Bar chart showing average bulk gas composition (molar fraction) of the sampled wells for the hydrocarbon-rich fields (Ratherford and Tocito Dome) and helium-rich fields (Navajo Springs, Pinta Dome, and Dineh-Bi-Keyah).

dominated given the lack of strong mantle components in helium, neon and argon isotopes, but instead is a signal from sedimentary organic matter in the mature window (Zhu et al., 2000). A mature zone is corroborated by hydrocarbon (gas wetness versus $\delta^{13}C$ (CH_4)) data (Fig. 7).

5.2.2. *Helium-rich fields*

High helium samples from the Dineh-Bi-Keyah, Pinta Dome, and Navajo Springs fields plot in the areas predicted for denitrification of post – mature organic sediments zone (+4‰ to +18‰), ammonium-rich clays (+1 to +4‰), and low temperature metamorphism of the crust (0‰ to +10‰) (Fig. 5) (Kreulen and Schuiling, 1982; Haendel et al., 1986; Bebout and Fogel, 1992; Bebout et al., 1999; Zhu et al., 2000; Cartigny and Marty, 2013; and Danabalan, 2017). Differentiation of sources is challenging because both metamorphosed rocks (up to greenschist) and modern sediments (+4 to 18‰) are marked by similar $\delta^{15}N$ ranges (Haendel et al., 1986; Zhu et al., 2000; Boyd, 2001; Cartigny and Marty, 2013; and Danabalan, 2017).

In the case of the Dineh-Bi-Keyah Field, organic N_2 may be partially related to hydrocarbon maturity as the samples plot in the post – mature gas window of carbon isotopes (Fig. 7). Although the Dineh-Bi-Keyah samples fall in the organic range, we neglect this process as a dominant mechanism due to the minute amounts of hydrocarbons measured in the samples (~1% CH_4) (Fig. 2). Furthermore, the influence of nitrogen derived from denitrification of post-mature organic matter is assumed to be insignificant for the Navajo Springs and Pinta Dome samples due to the lack of substantial hydrocarbon production and average 0.5% CH_4 in the gas stream.

The influence of ammonium (NH_4^+) ions held in clays can be significant if the correct geologic conditions are present, which are extreme temperature regimes (>500 °C) and/or fluid rock chemical interactions with highly saline brines (Williams et al., 1995; Mingram et al., 2005; Danabalan, 2017). Since there are documented intrusions in the Dineh-Bi-Keyah Field, the ammonium release scenario should be considered along with contributions from low temperature metamorphism of crustal basement rocks. Given the lack of igneous activity with Navajo Springs and Pinta Domes sampling areas, it is likely that the source of nitrogen is from low temperature metamorphism ($\delta^{15}N$ (N_2) 0 to +10‰) of the crustal basement rocks, such as nitrogen fixed in K feldspar and biotite in the shallow crystalline basement rocks. Furthermore, given the strong co-occurrence of ^4He—N_2 in Fig. 4, and the observation that ^4He is mostly crustal sourced, it is reasonable to assume the N_2 must also be derived from a crustal source, a crystalline basement or metasedimentary endmember (Ballentine and Sherwood-Lollar, 2002; Jenden et al., 1988).

Pursuing the plausibility of metasediment contribution from the underlying basement, median distance from sampled reservoirs to the basement top (for fields with helium >0.3%) was determined to be ~300 m, corroborating the basement as a highly plausible source based on proximal location. The presence of large basement faults and shear zones in the areas near high He/N_2 accumulations (Fig. 1) indicate that primary migration of the He/N_2 could be initiated with the release of the gas dissolved in solution from the source rocks via deep faulting, igneous intrusions, or other mechanisms (possibly from regional tectonic uplift and subsequent depressurization), which increase the permeability of the granitic host body (Sorenson, 2005; Sims et al., 2008; Torgersen, 2010; Danabalan et al., 2022). With deep faults acting as migration conduits, the basement sourced helium and nitrogen are subject to advection vertically (i.e., primary migration) through the overlying sedimentary packages followed by updip secondary lateral migration.

5.3. *Groundwater derived noble gases (^{20}Ne, ^{36}Ar)*

Atmosphere (air) derived noble gases (i.e., ^{20}Ne, ^{36}Ar, ^{84}Kr, and ^{130}Xe) are dissolved in groundwater according to their solubility coefficients. This process introduces noble gases in the form of air saturated water (ASW), into the subsurface through aquifer recharge. If groundwater comes into contact with a hydrocarbon phase, the noble gases will partition into oil or gas (Barry et al., 2016, 2017, 2018a). These noble gases can be harnessed as geochemical tracers and used as a gauge to measure the degree of reservoir and groundwater interaction (Ballentine and O'Nions, 1994; Pinti and Marty, 2000; Ozima and Podosek, 2002; Gilfillan et al., 2008; Zhou et al., 2012; Prinzhofer, 2013; and Byrne et al., 2017).

Moderate positive correlations are observed between ^{20}Ne and ^4He (Fig. A.3). This agrees with the findings of previously published work by Ballentine and Sherwood-Lollar, 2002, Danabalan (2017) and Danabalan et al., (2022), which showed an inherent relationship of positive correlations between ^4He and ^{20}Ne, (i.e., mixing before the groundwater essentially degassed the noble gases into the subsurface reservoirs). Moderate-weak positive correlations also exist between ^{36}Ar and ^4He (ASW and radiogenically derived isotopic components), which suggests mixing prior to degassing for the He-rich samples (Danabalan, 2017, Danabalan et al., 2022; Fig. A.3). The first order observation is that the highest ^4He is observed where there is the highest ^{36}Ar, indicating that the same process could be influencing both, presumably gas migration via groundwater or we may be observing decoupled systems.

5.4. *Fractionation processes*

Hydrocarbon and crustal gases acquire their initial atmospheric noble gas signatures through interaction with groundwater. Because each noble gas has a different solubility, the degree that ASW noble gases have interacted with groundwater can be quantified based on their respective fractionation ratios. Since the noble gases are geochemically inert, any fractionation can be interpreted to be the result of physical processes such as phase partitioning and migration (Ballentine et al., 2002).

Table 2
Isotopic gas values, R: Ratherford, TD: Tocito Dome, NS: Navajo Springs, PD: Pinta Dome, & DBK: Dineh-Bi-Keyah.

ID	$\frac{3_{He}}{4_{He}}$ R/R_a	± R_a	^{4}He µcm^3/cm^3	± µcm^3/cm^3	^{20}Ne µcm^3/cm^3	± µcm^3/cm^3	$\frac{20_{Ne}}{22_{Ne}}$	±	$\frac{21_{Ne}}{22_{Ne}}$	±	$\frac{20_{Ne}}{36_{Ar}}$	±	$\frac{38_{Ar}}{36_{Ar}}$	±
R12–23	0.03	2.12E-03	326.61	2.34	0.20	1.80E-03	9.77	0.03	0.03	1.12E-04	0.36	3.41E-03	0.20	7.87E-04
R13–41	0.03	6.84E-04	437.35	2.83	0.08	8.86E-04	9.75	0.02	0.03	1.11E-04	0.19	2.16E-03	0.20	8.13E-04
R20–66	0.03	8.41E-04	441.25	3.69	0.12	1.05E-03	9.76	0.03	0.03	1.11E-04	0.22	1.91E-03	0.19	7.03E-04
R20–42	0.03	6.98E-04	302.04	2.23	0.04	4.36E-04	9.77	0.03	0.03	1.32E-04	0.12	1.30E-03	0.20	5.87E-04
R20–44	0.04	1.37E-03	375.23	3.26	0.05	5.45E-04	9.74	0.03	0.03	1.15E-04	0.13	2.43E-03	0.20	7.51E-04
R29–31	0.03	3.41E-03	312.00	1.15	0.13	1.18E-03	9.73	0.02	0.03	1.24E-04	0.23	2.15E-03	0.18	7.35E-04
R15–33	0.09	1.39E-03	1057.62	10.25	0.22	2.74E-03	9.77	0.03	0.03	1.18E-04	0.21	2.88E-03	0.19	7.09E-04
R16–41	0.03	4.76E-03	242.68	1.63	0.04	5.98E-04	9.67	0.03	0.03	1.15E-04	0.13	1.73E-03	0.20	6.99E-04
R10–14	0.05	5.25E-03	404.22	2.98	0.07	6.95E-04	9.72	0.03	0.03	1.09E-04	0.18	1.80E-03	0.19	7.70E-04
R10–32	0.03	2.47E-03	619.69	4.19	0.07	6.25E-04	9.80	0.03	0.04	1.48E-04	0.21	2.00E-03	0.20	7.69E-04
R9–34	0.02	1.72E-03	145.97	1.27	0.01	1.24E-04	9.77	0.03	0.05	1.69E-04	0.15	1.42E-03	0.20	7.14E-04
R17–13	0.03	1.71E-03	172.95	0.98	0.01	1.50E-04	9.76	0.03	0.03	1.32E-04	0.12	1.37E-03	0.20	7.69E-04
R17–11	0.02	5.25E-04	317.92	1.90	0.06	5.47E-04	9.76	0.03	0.03	1.11E-04	0.14	1.21E-03	0.20	7.95E-04
R17–22	0.02	1.24E-03	253.00	1.71	0.07	6.28E-04	9.76	0.03	0.04	1.49E-04	0.15	1.45E-03	0.20	7.87E-04
R13–12	0.06	3.56E-03	300.07	2.54	0.11	9.88E-04	9.72	0.03	0.03	1.07E-04	0.22	1.89E-03	0.20	1.02E-03
TD U 9	0.07	2.21E-03	3572.48	12.75	0.10	7.86E-04	9.64	0.03	0.04	1.40E-04	0.37	2.99E-03	0.20	7.23E-04
TD U 7	0.09	8.04E-03	4255.31	20.29	0.10	9.89E-04	9.82	0.03	0.04	1.56E-04	0.37	3.63E-03	0.19	7.14E-04
TD U 12	0.08	7.94E-03	4120.84	24.19	0.03	3.47E-04	9.58	0.02	0.05	1.91E-04	0.10	1.17E-03	0.20	9.71E-04
TD N 1	0.09	7.30E-03	5213.49	45.20	0.05	4.56E-04	9.70	0.03	0.04	1.77E-04	0.13	1.30E-03	0.20	7.45E-04
TD N 11	0.08	7.75E-03	6071.28	16.81	0.03	2.97E-04	9.74	0.03	0.06	2.22E-04	0.18	1.54E-03	0.20	5.86E-04
TD N 6	0.09	3.57E-03	3533.09	13.24	0.12	9.41E-04	9.48	0.02	0.05	1.31E-04	0.32	2.54E-03	0.19	6.89E-04
NS 31–1	0.18	6.25E-03	63,983.85	271.73	5.68	5.57E-02	9.34	0.02	0.04	1.49E-04	1.93	2.46E-02	0.19	6.81E-04
PD 33–1	0.20	8.24E-03	63,086.58	460.97	3.07	2.73E-02	9.21	0.02	0.04	1.42E-04	0.94	1.16E-02	0.19	6.92E-04
PD 34–1	0.22	3.44E-03	79,200.32	778.51	3.18	3.52E-02	9.72	0.02	0.05	1.88E-04	0.65	1.05E-02	0.19	1.02E-03
DBK B 2	0.05	3.19E-03	50,390.09	125.32	3.69	3.83E-02	9.38	0.02	0.06	1.97E-04	3.45	3.69E-02	0.19	7.33E-04
DBK C 2	0.06	8.88E-03	73,308.20	230.17	2.48	2.65E-02	9.21	0.02	0.08	3.07E-04	1.68	2.27E-02	0.19	8.49E-04
DBK 4	0.07	7.23E-03	55,001.97	193.44	1.12	1.13E-02	9.41	0.02	0.08	2.98E-04	2.50	2.65E-02	0.19	6.95E-04
DBK 24	0.06	1.70E-03	57,579.14	418.54	1.44	1.52E-02	9.30	0.02	0.08	2.96E-04	1.13	1.43E-02	0.20	7.39E-04
DBK 15	0.07	5.40E-03	54,990.64	257.91	2.85	3.56E-02	9.58	0.02	0.07	2.80E-04	1.75	2.29E-02	0.20	7.01E-04
DBK 88 3	0.07	2.41E-03	59,370.42	205.96	2.81	2.75E-02	9.46	0.02	0.07	2.81E-04	1.68	2.21E-02	0.18	6.73E-04
DBK 88 2	0.06	3.07E-03	61,397.38	513.09	0.29	2.72E-03	9.30	0.02	0.05	1.84E-04	0.52	5.12E-03	0.19	9.71E-04

ID	$\frac{40_{Ar}}{36_{Ar}}$	±	^{84}Kr ncm^3/cm^3	± ncm^3/cm^3	^{132}Xe ncm^3/cm^3	± ncm^3/cm^3	$\frac{86_{Kr}}{84_{Kr}}$	±	$\frac{132_{Xe}}{130_{Xe}}$	±	δ^{15}N ‰	± Per mil	δ^{13}C ‰ CH_4	± Per mil
R12–23	355.77	0.99	20.16	0.30	0.96	0.01	0.30	1.19E-03	6.53	2.55E-02	−6.85	0.20	−49.74	0.09
R13–41	528.67	1.65	13.38	0.19	0.54	0.01	0.30	8.39E-04	6.54	2.33E-02	−8.81	0.19	−48.47	0.09
R20–66	434.11	0.84	27.73	0.35	1.17	0.02	0.30	9.43E-04	6.52	1.99E-02	−4.92	0.25	−49.12	0.08
R20–42	555.25	1.38	18.19	0.23	1.60	0.02	0.31	7.95E-04	6.49	2.14E-02	−3.68	0.20	−51.67	0.08
R20–44	524.14	1.95	12.18	0.20	0.73	0.01	0.30	7.56E-04	6.55	1.95E-02	−9.28	0.18	−46.24	0.08
R29–31	408.69	1.21	16.66	0.24	0.69	0.01	0.30	8.68E-04	6.54	2.10E-02	−3.54	0.16	−47.05	0.10
R15–33	823.85	2.17	48.35	0.69	2.80	0.03	0.30	8.53E-04	6.46	1.88E-02	−7.30	0.28	−48.86	0.09
R16–41	550.22	1.48	18.40	0.25	1.00	0.01	0.30	8.03E-04	6.54	1.90E-02	−6.54	0.29	−48.26	0.09
R10–14	513.11	1.19	18.19	0.28	0.90	0.01	0.31	8.72E-04	6.52	2.18E-02	−11.68	0.19	−53.63	0.08
R10–32	694.54	1.94	10.12	0.13	0.04	0.00	0.30	7.78E-04	6.49	2.61E-02	−7.17	0.17	−48.98	0.09
R9–34	529.83	1.59	1.25	0.02	0.12	0.00	0.31	9.10E-04	6.52	2.11E-02	−8.64	0.18	−51.10	0.09
R17–13	505.54	1.15	2.45	0.03	0.23	0.00	0.30	7.51E-04	6.38	2.14E-02	−7.09	0.20	−48.76	0.10
R17–11	493.22	1.17	20.70	0.27	0.79	0.01	0.30	6.28E-04	6.58	2.24E-02	−3.48	0.20	−49.69	0.09
R17–22	454.44	1.94	5.95	0.09	0.87	0.01	0.30	8.78E-04	6.56	2.55E-02	−4.60	0.15	−50.21	0.08
R13–12	465.53	1.20	8.01	0.19	0.47	0.00	0.31	8.12E-04	6.57	2.20E-02	−2.48	0.19	−49.57	0.09
TD U 9	2994.02	6.55	3.69	0.04	0.52	0.01	0.30	8.46E-04	6.56	2.53E-02	−4.74	0.27	−45.77	0.08
TD U 7	2968.43	7.09	17.11	0.24	0.63	0.01	0.30	8.46E-04	6.50	2.37E-02	−3.16	0.24	−44.74	0.08
TD U 12	2811.86	8.32	15.62	0.22	1.67	0.02	0.30		6.50		−5.74	0.17	−46.85	0.09

(*continued on next page*)

Table 2 (*continued*)

ID	$\frac{40_{Ar}}{36_{Ar}}$	±	^{84}Kr ncm^3/cm^3	± ncm^3/cm^3	^{132}Xe ncm^3/cm^3	± ncm^3/cm^3	$\frac{86_{Kr}}{84_{Kr}}$	±	$\frac{132_{Xe}}{130_{Xe}}$	±	δ^{15}N ‰	± Per mil	δ^{13}C ‰ CH_4	± Per mil
								8.43E-04		2.65E-02				
TD N 1	2550.44	5.17	12.70	0.17	3.03	0.04	0.31	9.16E-04	6.39	4.18E-02	−6.87	0.18	−45.13	0.09
TD N 11	5177.45	10.61	7.75	0.09	2.01	0.02	0.30	9.23E-04	6.50	1.99E-02	−8.03	0.27	−43.00	0.08
TD N 6	2962.29	8.76	6.74	0.07	0.68	0.01	0.30	1.04E-03	6.47	1.96E-02	−4.41	0.27	−44.04	0.10
NS 31–1	2167.53	5.67	72.65	0.88	6.64	0.07	0.30	8.09E-04	6.45	2.11E-02	4.65	0.23	−34.71	0.13
PD 33–1	1291.91	3.15	74.39	0.79	5.97	0.06	0.30	1.04E-03	6.56	1.94E-02	5.99	0.27	−33.74	0.12
PD 34–1	4730.65	13.58	120.89	1.51	11.38	0.11	0.30	7.83E-04	6.51	2.60E-02	3.17	0.18	−31.12	0.12
DBK B 2	16,191.00	20.22	23.92	0.35	7.64	0.08	0.30	8.13E-04	6.56	3.11E-02	5.99	0.29	−30.57	0.08
DBK C 2	15,747.38	25.65	58.70	0.63	9.32	0.09	0.30	8.33E-04	6.59	2.14E-02	2.97	0.26	−35.94	0.08
DBK 4	15,893.38	30.65	17.45	0.29	3.30	0.04	0.30	6.34E-04	6.53	2.61E-02	7.64	0.18	−36.19	0.09
DBK 24	17,083.19	15.87	48.16	0.59	8.78	0.09	0.30	8.11E-04	6.55	3.04E-02	3.02	0.20	−31.74	0.10
DBK 15	13,872.28	34.25	72.35	0.77	18.20	0.23	0.30	8.04E-04	6.44	3.57E-02	4.87	0.22	−33.88	0.10
DBK 88 3	13,652.54	36.84	70.21	0.80	17.74	0.19	0.31	8.32E-04	6.48	3.92E-02	6.87	0.25	−31.79	0.09
DBK 88 2	12,217.41	29.55	23.24	0.25	5.72	0.08	0.30	7.48E-04	6.33	5.31E-02	7.23	0.24	−35.77	0.08

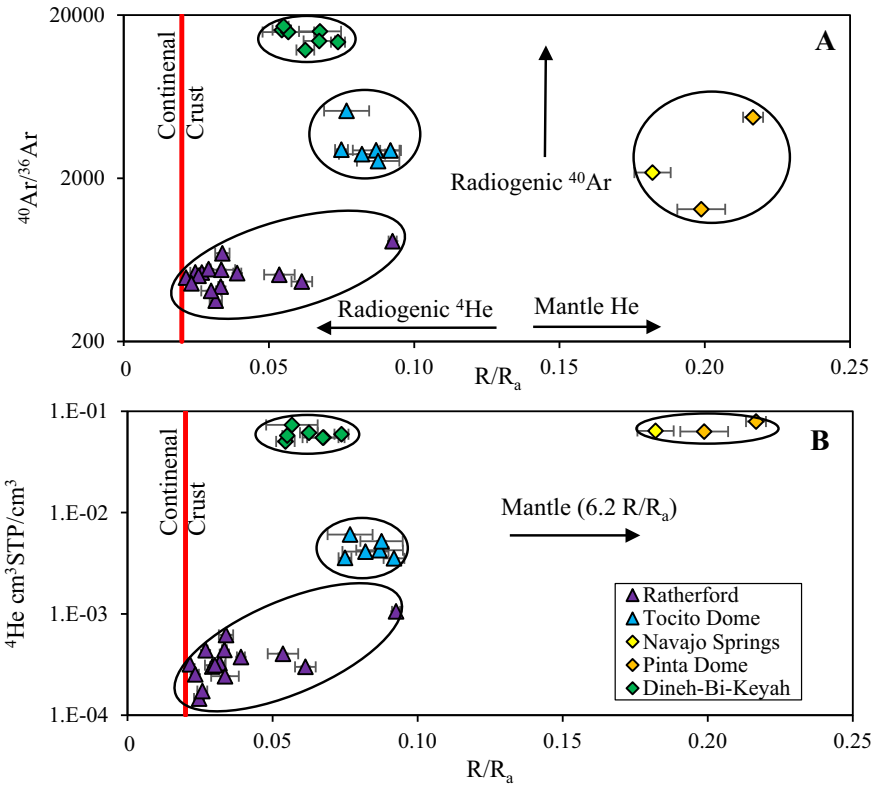

Fig. 3. Cross plots illustrating four unique groupings of gas families. 3A) R/R$_a$ versus ^{40}Ar/^{36}Ar and 3B) R/R$_a$ versus ^{4}He both showing the influence of crustal and mantle components. The red line indicates the crustal R/R$_a$ signature. Continental crust signature is 0.02 (Andrews, 1985; Ballentine and Burnard, 2002; Boreham et al., 2018). Error bars are smaller than symbols for ^{4}He and ^{40}Ar/^{36}Ar. He-rich fields are represented with diamonds, whereas the hydrocarbon–rich fields are represented with triangles. (For interpretation of the references to colour in this figure legend, the reader is referred to the web version of this article.)

Furthermore, if a migrating gas phase encounters a groundwater with gases dissolved in solution, dissolved ASW gases can be effectively exsolved from the solution back into the gas phase (Brown, 2010). This might occur when gas dissolved in pore water begins to move laterally within the reservoir. Exsolution might also be plausible given a change in pressure in the absence of a migrating carrier gas (Ballentine et al., 2002; Danabalan et al., 2022).

5.4.1. *Oil-water system*

To understand noble gas fractionation of hydrocarbon-rich systems,

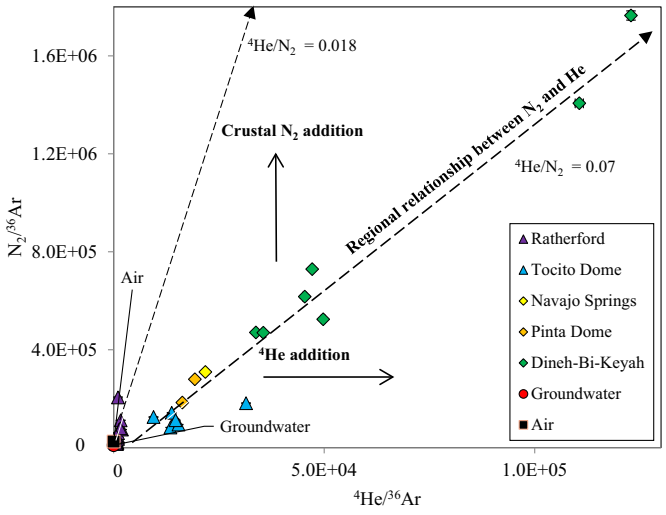

Fig. 4. ^{4}He/^{36}Ar versus N$_2$/^{36}Ar plot, showing two groups – He-rich fields with a regional ^{4}He/N$_2$ ratio of 0.07, and a hydrocarbon-rich field (e.g., Ratherford), which has a shallow-sourced N$_2$ end member and ^{4}He/N$_2$ ratio of 0.018. Groundwater and air values are calculated from Kennedy and Truesdell (1995); Marty et al. (1996); Marty et al. (2013).

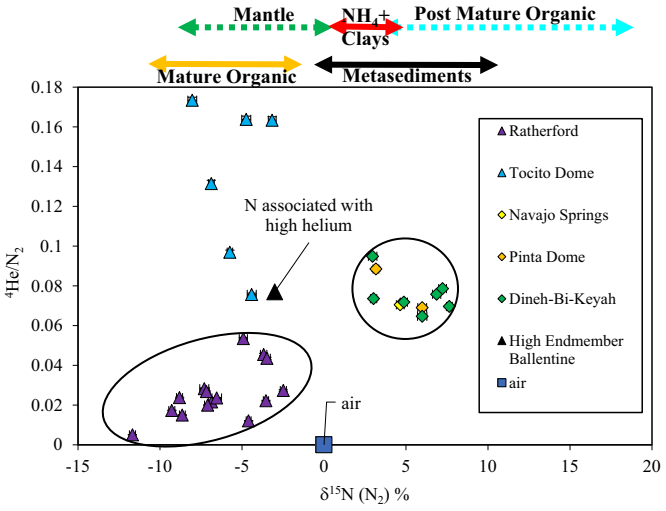

Fig. 5. Plot of ^{4}He/N$_2$ versus δ^{15}N (N$_2$) ‰ showing crustal N$_2$ (metasediments/clays) is the primary source of He-rich associated N$_2$. High end-member, which represents the highest ^{4}He/N$_2$ sample measured in the Hugoton Panhandle Texas system, is from Ballentine and Sherwood-Lollar (2002); air is from Labidi et al., (2020). δ^{15}N (N$_2$) ranges are from Cartigny and Marty (2013), Danabalan (2017); and Danabalan et al., (2022). Error bars are smaller than symbols (^{4}He/N$_2$).

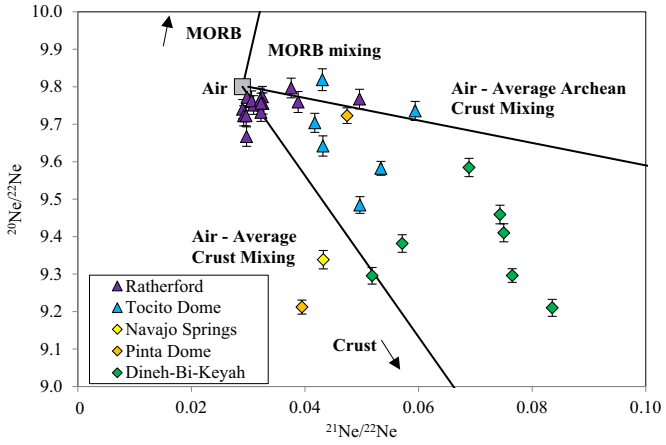

Fig. 6. Neon plot supporting a strong crustal component mixing with air. Error bars are smaller than printed symbols for ^{21}Ne/^{22}Ne (Ballentine and O'Nions, 1992; Ballentine and Burnard, 2002; Ballentine and Holland, 2008; Warr et al., 2018; Li et al., 2020).

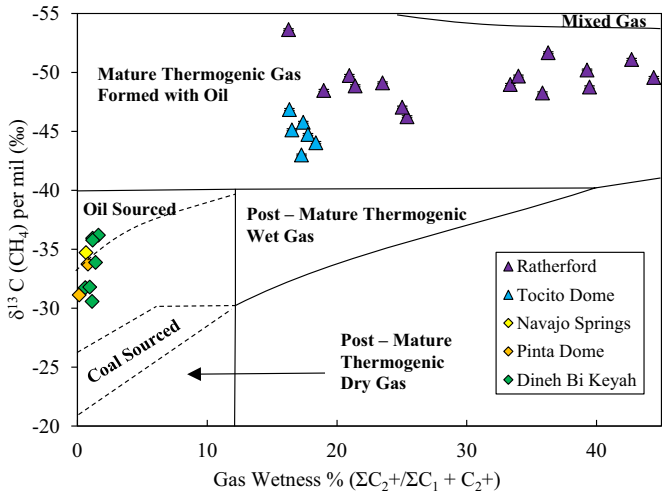

Fig. 7. δ^{13}C(CH$_4$) versus gas wetness % ($(\Sigma C_{2+})/\Sigma(C_1 + C_{2+})$) showing data plotted in the approximate ranges of gas composition related to post mature – dry gas, post mature wet gas, mixed gas, and mature gas formed with oil (Schoell, 1983, 1988; Faber et al., 1992; Whiticar et al., 1994; Ellis, 2014; Travers et al., 2014; Selley and Sonnenberg, 2015). The error bars for gas wetness are smaller than the symbols.

we present a two-stage equilibrium fractionation and air mixing model, which shows the hydrocarbon-rich samples of the Ratherford and Tocito Dome plotting between ASW and air endmembers (Fig. 8 A&B) (Barry et al., 2016). A prior assumption is that oil is noble gas free before equilibrating with water (Ballentine et al., 2002). For stage 1, oil and water are assumed to equilibrate within a closed system (Eqs. A.1 and A.2). The oil equilibration with water curve (Fig. 8A&B) shows the predicted evolution of the oil phase at different oil/water ratios (Barry et al., 2018b). The predicted evolution of the oil phase at different oil/water ratios (from infinitesimally small to large) is presented for two temperatures of 325 K and 345 K corresponding to averages for the Ratherford and Tocito Dome fields (Rutledge, 2010; Ballentine et al., 2002). The binary mixing lines (purple – Ratherford; blue – Tocito Dome) represents stage 2, binary mixing with an atmospheric component, showing ~1% air (Ratherford) and 0.5% air (Tocito Dome) admixture into the subsurface system (Eq. A.3), which is likely the result of secondary recovery waterfloods (Freeman, 1978; Spencer, 1978). However, the model does not only apply to reservoirs impacted by waterflooding.

Ratherford and Tocito Dome field parameters are shown in Tables A.2, A.3, A.4, and A.5 in the appendix. Measured noble gas concentrations in cm^{3}STP/cm^3 (in the gas phase) are converted into the oil phase in mol kg/mol using Eq. A.2 (Barry et al., 2018b). GOR $_{metric}$ (gas to oil ratios) are incorporated from production reports and minimal values are chosen to represent pristine reservoir conditions (Barry et al., 2018b).

In Fig. 8 A&B, we observe ^{20}Ne/^{36}Ar and ^{20}Ne values above the oil-water equilibration line for Ratherford and Tocito Dome samples. We postulate that this signal is air derived. The retention of a gas phase (either from degassing from production or secondary charging/mixing episodes) is the opposite scenario to what was observed in Barry et al.

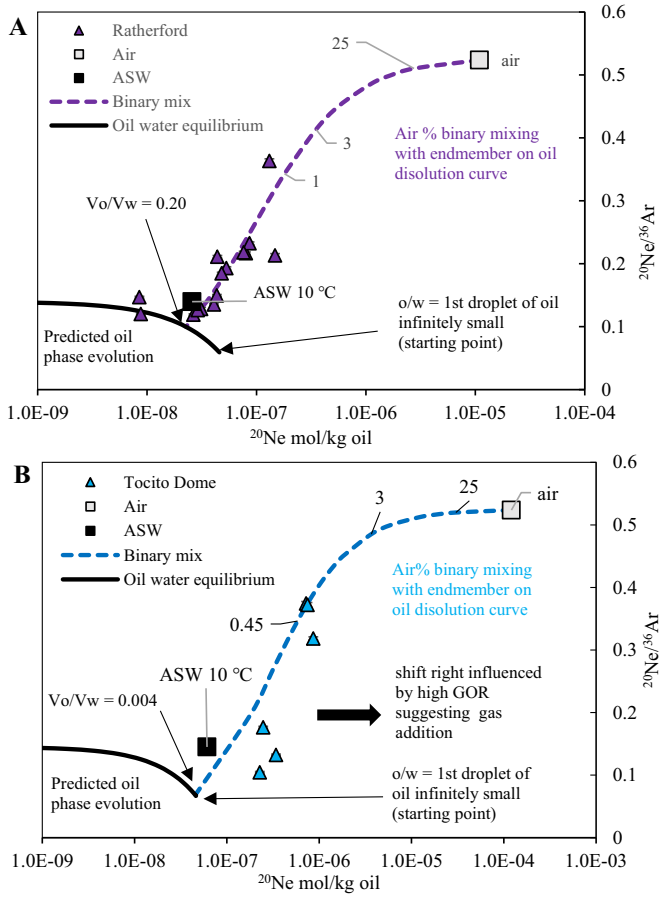

Fig. 8. $^{20}Ne/^{36}Ar$ fractionation as the result of batch closed system fractionation (oil equilibration with water) and binary mixing between air in Ratherford (A) and Tocito Dome (B) fields. Dashed lines show mixing with air, percent of air in the mixture is annotated.

(2018b). The gas addition/retention narrative conforms agreeably with gas cap calculations for Ratherford and the Tocito Dome, which indicate there is no initial gas cap using virgin GORs (i.e., minimum GOR), and any significant gas volumes produced since initial drilling have resulted from the decrease in reservoir pressure (Barry et al., 2018b) (Table A.8). The lowest (virgin) GOR value was chosen as a best estimate due to a lack of initial production (IP) values. Additionally, an average GOR that is measured at the wellhead was not utilized as it will not necessarily be the most characteristic sample of initial GOR conditions, and will change over time with production fluctuations (Barry et al., 2018b).

By utilizing the natural gas isotope data to inform our field simulations, we model these two fields as a two-component water-oil system mixing with air. The two-phase oil fractionation model presents binary mixing curves with end points chosen on the oil water equilibration line to incorporate the largest number of data points. The model assumes oil moves through water to acquire the noble gas signature in stage one. Stage two assumes that equilibration of oil and dissolved noble gases occur with air (Fig. 9). It is also important to note that for these oil systems, hydrocarbons do not seem to contribute positively to considerable high helium accumulations and are therefore potentially diluting the helium content of the system.

5.4.2. Gas-water system

The He-rich samples of Navajo Springs, Pinta Dome, and Dineh-Bi-Keyah fields display $^{20}Ne/^{36}Ar$ ratios between 0.5 and 3.5, ranging to significantly above the value of air (0.52) and the maximum values possible through simple closed or open system equilibration with water (Barry et al., 2016). High values of $^{20}Ne/^{36}Ar$ have been previously

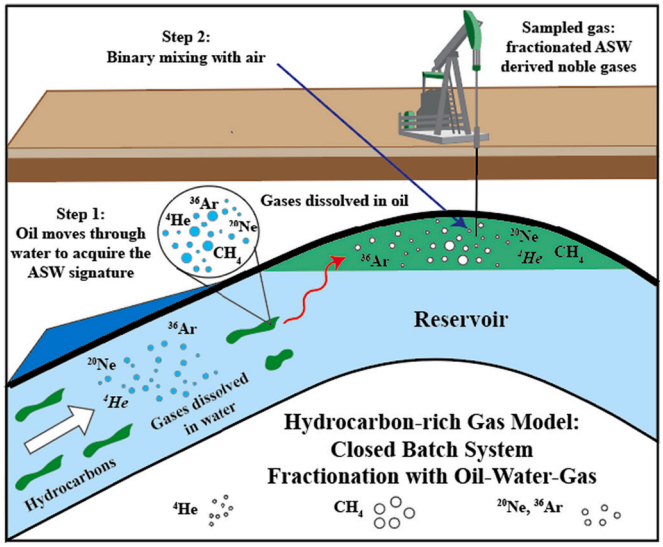

Fig. 9. Schematic illustrating the conceptual two-stage equilibration model (closed batch system fractionation) devoid of an initial gas cap that explains the Ratherford and Tocito Dome hydrocarbon-rich samples by a two-step approach where 1) oil moves through water to acquire the ASW signatures and 2) binary mixing with air occurs.

reported to result from gas dissolution in water in an open system (Gilfillan et al., 2008; Darrah et al., 2014) due to the lower solubility of ^{20}Ne relative to ^{36}Ar. We assume that atmospheric noble gases were fully exsolved from water by a migrating N_2 phase, resulting in a gas phase with a $^{20}Ne/^{36}Ar$ ratio equal to that of ASW. Subsequently, the gas phase is redissolved into the noble gas free water in an open system, following Eq. 1 (Ballentine et al., 2002). Noble gas concentrations are therefore controlled by their solubility and the solubility of the carrier gas phase (N_2).

In a simple system, where the gas phase re-equilibrates with a column of water that is controlled by N_2 dissolution, we would expect the measured $^{20}Ne/^{36}Ar$ and $^{4}He/N_2$ ratios to plot on the open system Rayleigh curves with N_2 as a carrier gas (Eq. A.15) (Ballentine et al., 2002; Barry et al., 2016) (Fig. 10A). The Rayleigh curves were modelled using N_2 solubility values from the IUPAC solubility data series vol. 10 – Battino et al. (1982) and Gevantman (1992). The liquid phase activity coefficient is derived from Table 6 in Valderrama et al. (2016). The gas phase fugacity coefficient is derived by calculating the fugacity of N_2 divided by the pressure ($\phi = f/p$); the complete fugacity equation is listed in the appendix (Eq. A.4) (Atkins and De Paula, 2006). Our data plot significantly above and below the modelled N_2 dissolution lines, indicating that the $^{20}Ne/^{36}Ar$ and $^{4}He/N_2$ are decoupled, the latter being unaffected by high degrees of re-dissolution into shallow groundwater systems.

$$\left(\frac{[i]}{[N_2]}\right) = \left(\frac{[i]}{[N_2]}\right)_o P^{\left(\frac{1}{\alpha}-1\right)} \quad (1)$$

where $i = {}^4He$, ^{20}Ne, and ^{36}Ar, α is the fractionation coefficient = $(\gamma i/\phi i \times Ki^{groundwater})/(\gamma_{N2}/\phi_{N2} \times K_{N2}{}^{groundwater})$, where K = Henry' s constant Gpa, γ_i/ϕ_i = (liquid phase activity coefficient)/(gas phase fugacity coefficient), $([i]/[N_2])_o$ = original ratio, and p = the fraction of N_2 remaining in the water phase.

$$\left(\frac{[20_{Ne}]}{[36_{Ar}]}\right)_g = \left(\frac{[20_{Ne}]}{[36_{Ar}]}\right)_{og} P^{\left(\frac{1}{\alpha}-1\right)} \quad (2)$$

where α is the fractionation coefficient = $(\gamma_{20Ne}/\phi_{20Ne} \times K_{20Ne}{}^{groundwater})/(\gamma_{36Ar}/\phi_{36Ar} \times K_{36Ar}{}^{groundwater})$, $([^{20}Ne]/[^{36}Ar])_{og}$ = original

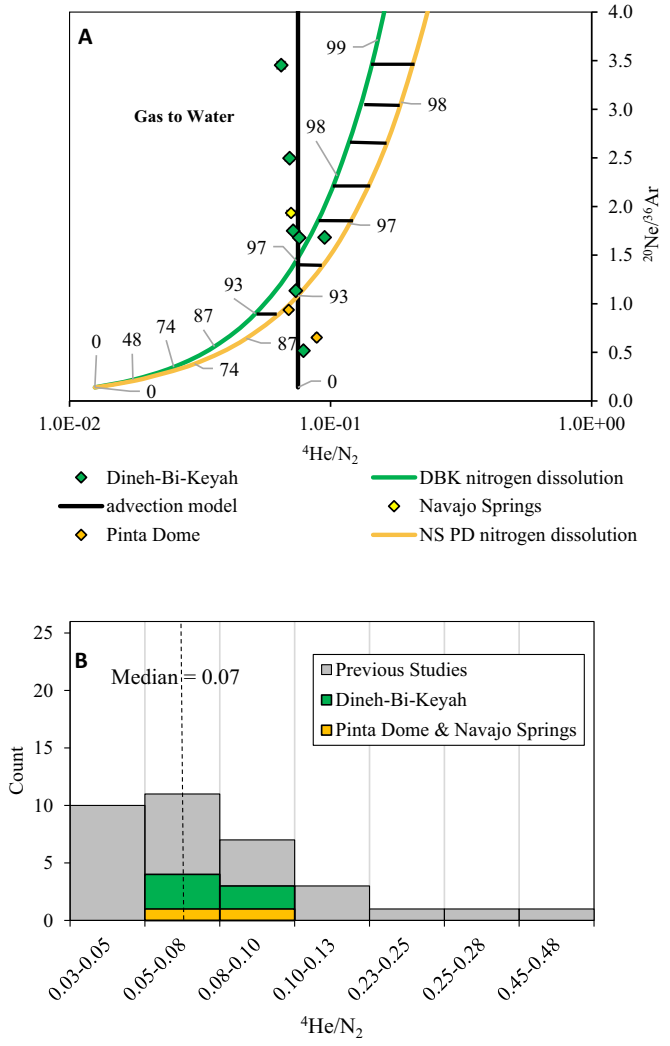

Fig. 10. A&B: A) He-rich model showing 1) the green and gold curves represent Rayleigh open system fractionation models with N_2 as the primary carrier gas, which is dissolving back into a groundwater solution. The gold curve is modelled with the Pinta Dome and Navajo Springs parameters (Tables A.2, A.3, and A.6); the green curve is modelled with Dineh-Bi-Keyah parameters (Tables A.2, A.3, and A.7). Horizontal black lines between the gold and green curves indicate a potential range of the best fit data. Starting $^4He/N_2$ values were chosen to yield a best fit, and the starting $^{20}Ne/^{36}Ar$ value is 0.14 (ASW). 2) A black line representing an advection based model based on a constant $^4He/N_2$ ratio determined by the median value in Fig. 4B (0.075), and a Rayleigh open system fractionation model in the $^{20}Ne/^{36}Ar$ space. B) Histogram of He-rich samples and previous data (Craddock et al., 2017; Gilfillan et al., 2008). (For interpretation of the references to colour in this figure legend, the reader is referred to the web version of this article.)

groundwater phase ratio, and p = the fraction of Ar remaining in the water phase.

Despite the large fractionation in the $^{20}Ne/^{36}Ar$, the $^4He/N_2$ in He-rich samples are nearly constant (Fig. 10A). The observed $^4He/N_2$ are consistent with median values observed in previous studies on the Colorado Plateau (Fig. 10B), indicating that the measured $^4He/N_2$ likely reflects an unfractionated production ratio likely influenced by an advection-based basement flux (Zhou and Ballentine, 2006). The re-dissolution process (Eq. 2 – Ballentine et al., 2002) therefore seems to only affect the atmospheric noble gases and not the N_2 and He contents of the gas phase (solid black line, Fig. 10A).

Fig. 11 presents a four-stage box model, which incorporates a decoupled dynamic gas phase migration of ^4He and N_2 from the basement (primarily through advection processes) along with a secondary lateral ^{20}Ne and ^{36}Ar migration controlled by groundwater and gas movement. The presence of local high angle basement faults and basement shear zones in the vicinity of high helium fields (Fig. 1) supports the hypothesis of faults acting as migration conduits (i.e., linking the basement source rock to the reservoir) and transporting ^4He and N_2 via advective fluid flow. The observed $^4He/N_2$ ratios likely reflect production ratios in the basement prior to mobilization (Karolytė et al., 2022).

Stage 1 represents the initial conditions where groundwater ^{20}Ne and ^{36}Ar ASW contents are in equilibrium with the atmosphere during the initial recharge conditions, and crustal N_2 and ^4He are dissolved in basement groundwater. The acquired concentrations of He and N_2 at atmospheric pressure are low and considered negligible relative to the concentrations acquired during the secondary equilibration at depth (N_2 carrier gas with He enrichment). Stage 2 signifies a period where the basement has been faulted and uplifted (as a result of inversion tectonics on the Colorado Plateau) (Davis and Bump, 2009) and a subsequent flux of N_2 and ^4He (advective fluid flow) is introduced into the overlying sedimentary column. N_2 and ^4He are degassed due to decompression, before migrating into the reservoir where the groundwater is stripped of its atmospheric noble gases, forming a gas cap above the water column (Sorenson, 2005; Torgersen, 2010; Danabalan et al., 2022). Gas cap calculations are in the appendix (section 6). The gases continue to exsolve into the gas cap in the reservoir and eventually all ASW-derived noble gases are stripped and the groundwater is saturated with respect to N_2 and ^4He (Stage 3). Finally, the gas cap begins re-equilibrating with the degassed water, likely through lateral gas migration or pressure change, and ASW-derived noble gases re-dissolve into groundwater, however ^4He and N_2 dissolution is prevented by oversaturation through continuous flux from the basement. The re-dissolution process only affects the atmospheric noble gases because their total budget in the subsurface is determined by equilibration with the atmosphere during water recharge (crustal fluids have no additional sources of ^{20}Ne and ^{36}Ar, therefore water will not be saturated in respect to these gases), while basement-sourced N_2 and He may occur in much higher volumes (depending on the volume of basement where fluids are liberated from) and therefore fully saturate the water column.

Several alternative mechanisms of $^{20}Ne/^{36}Ar$ fractionation are discussed (and ultimately discounted) in the appendix (section 5). These involve (1–2) oil contributions, (3) non-equilibrium diffusion, (4) multi-stage phase equilibrium fractionation, and (5) partial ASW redissolution with nitrogen as the carrier gas. Regarding option (3), there is little evidence for diffusion controlled isotopic fractionation in our samples (appendix section 5) (Fig. A.4), and thus we treat these subsurface systems as primarily advection-controlled systems (Caracausi and Paternoster, 2015; Buttitta et al., 2020; Lowenstern et al., 2014; Brown, 2010; and Tolstikhin et al., 2010).

5.5. Helium mass balance

To understand a regional helium system, we need to account for the amount of helium formed in different regions of the crust: 1) reservoir, 2) reservoir + underlying sediments, and 3) basement down to 10 km depth, as ~90% of the Earth's ^4He is generated in this interval (Ballentine and Burnard, 2002) (Fig. 12).

In order to better constrain the volume of helium that could be sourced internally from the reservoir or externally, helium mass balance calculations were made for the area directly under the field. By utilizing the average crustal occurrences of uranium (U) and thorium (Th) over discrete time intervals, we postulate the volume of the source rock required to generate the observed helium accumulations in the reservoirs.

5.5.1. In-situ helium production

To investigate the volumes of rock required to produce crustal gases

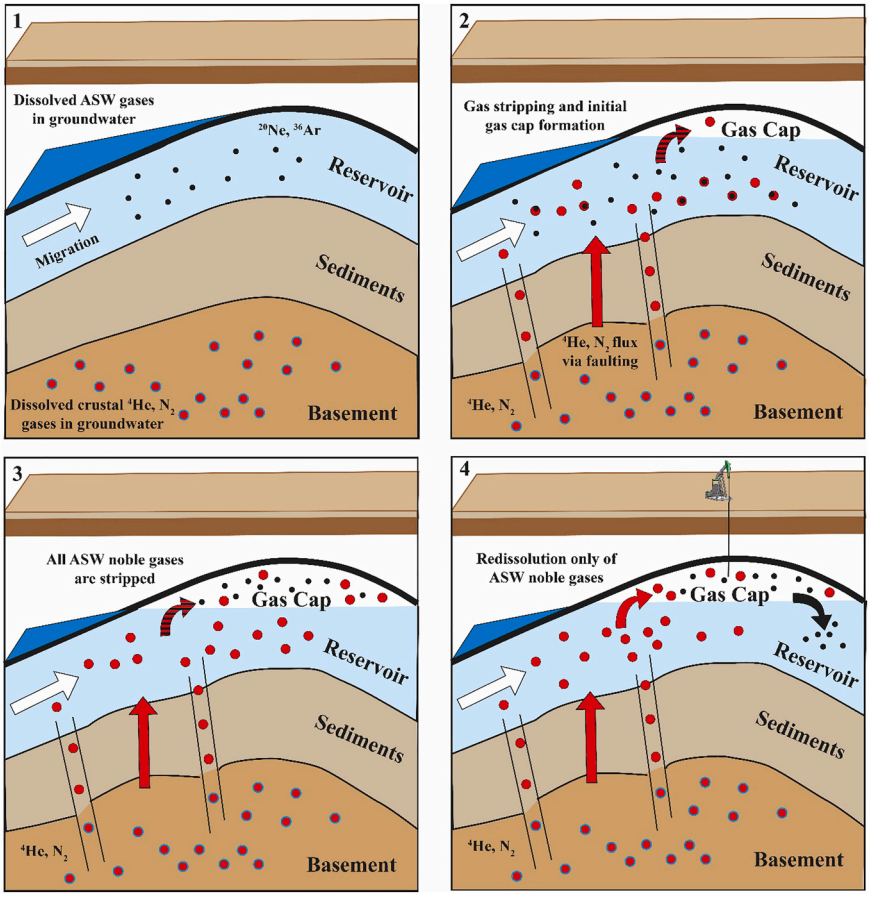

Fig. 11. Schematic illustrating the conceptual four-stage decoupled model which explains He signatures (advective fluid flow) and highly fractionated $^{20}Ne/^{36}Ar$ values (partial redissolution) of the Navajo Springs, Pinta Dome, and Dineh-Bi-Keyah fields. Stage 1 represents the initial conditions where groundwater ^{20}Ne and ^{36}Ar contents (black dots) are in equilibrium with the atmosphere during the initial recharge conditions, and N_2 and ^{4}He are dissolved in basement groundwater (red dots outlined in blue). Stage 2 signifies basement faulting and flux of N_2 and ^{4}He (advective fluid flow). N_2 and ^{4}He are degassed due to decompression, migrate into the reservoir and begin to strip the groundwater of atmospheric noble gases, forming a gas cap above the water column. Stage 3) gases continue to exsolve into the gas cap in the reservoir and eventually all ASW-derived noble gases are stripped and the groundwater is saturated in N_2 and ^{4}He. Stage 4) the gas cap begins re-equilibrating with the degassed water (lateral gas migration or pressure change), and ASW-derived noble gases re-dissolve into groundwater, however ^{4}He and N_2 dissolution is prevented by oversaturation through continuous flux from the basement. (For interpretation of the references to colour in this figure legend, the reader is referred to the web version of this article.)

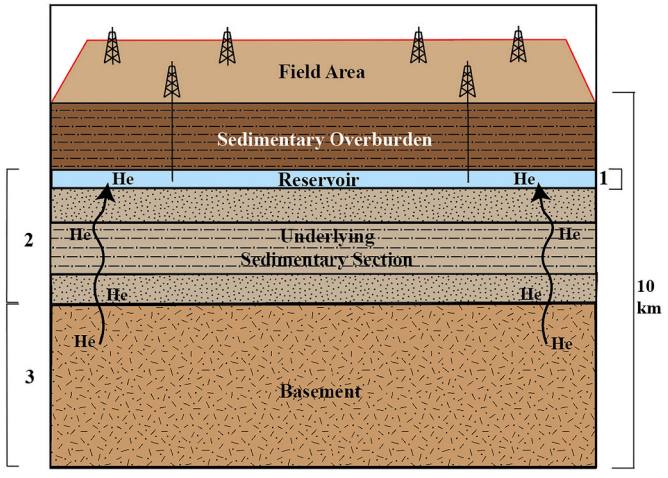

Fig. 12. Simplified illustration showing volumes of rock beneath the field, which were utilized for the mass balance calculations: 1.) reservoir, 2.) reservoir + underlying sediments, and 3.) basement. Figure not to scale.

that are needed to saturate the water and explain the observed helium signatures, we calculate the possible contribution of helium from the reservoir itself. As an aside, to supplement these calculations, additional hybrid models tying the in-situ mass balance models back to the multi-phase fractionation models to investigate required volumes of rock and required reservoir water are presented in the appendix for the hydrocarbon-rich fields (Tables A.9 and A.10).

Initial volumetric calculations, original gas in place (OGIP) and original helium in place (OHIP), are calculated for each field (Eq. 3; Tables A.11 and A.12). OGIP is defined as:

$$OGIP = \frac{Ah\phi(1 - S_W)}{1} \times \frac{Ts\ Pi}{Ps\ Tf\ Zi} \quad (3)$$

where OGIP cubic feet [meters^3], A is the reservoir area ft^2 [m^2], h is the net pay thickness ft. [m], ϕ is the porosity, S_w is the water saturation, T_s is the base temperature standard condition Rankine [Kelvin], P_i is the initial reservoir pressure psia [kPaa], P_s is the base pressure standard conditions 14.65 psia [101.35 kPaa], T_f is the formation temperature Rankine [Kelvin], Z_i is the compressibility at reservoir pressure and temperature of the dominant gas (Robinson and Peng, 1976), and (T_s Pi / P_s T_f Z_i) = B_{gi}, which is the initial conditions gas formation volume factor (Mireault et al., 2007). We assume that the volumes are at ambient temperature of 15 °C/ 60 °F and convert them to 0 °C/32 °F STP (based on the Ideal Gas Law).

In order to determine the in-situ helium contribution of each reservoir, the in-situ ^{4}He production is calculated based on the work of Ballentine and Burnard, 2002; Zhou and Ballentine, 2006; Danabalan, 2017; Karolytė et al., 2019; and Buttitta et al., 2020 (Eqs. 4 and 5). The amount of ^{4}He produced in atoms/g for a specified time interval is defined as:

$$^{4}He\frac{atoms}{grams} = X_R[R]\left(\frac{N_A}{A_R}\right) \times 10^{-6}\left(e^{\lambda t} - 1\right) \times yield_r \quad (4)$$

where X_R is the fractional natural abundance of isotope R, R is the concentration of R in ppm, N_A is the Avagadro's number (6.023×10^{23}), A_R is the molar mass of R (g), λ is the decay constant of R per year, t is the age in years, and $yield_r$ is the number of alpha particles emitted (Ballentine and Burnard, 2002). The amount of ^{4}He produced in-situ is defined as:

$$^4He \text{ atoms in situ} = p \times \bigwedge a \times (1 - \phi) \times V \quad (5)$$

where ^{4}He in-situ is the ^{4}He atoms, p is the average crustal rock density 2.7 g/cm^3, α is the ^{4}He atoms grams^{-1}, ⋀ is the efficiency of release, assumed to be 1, ϕ is the porosity, and V is the volume cm^3 (Buttitta et al., 2020).

Average crustal U and Th concentrations of 2.8 and 10.7 ppm are assumed (Burwash and Cumming, 1976; Danabalan et al., 2022). The residence time of all the fields, which is assumed to correlate with the time period after when the seal was deposited (± several million years), is assumed to be 300 Mya for the Ratherford, Tocito Dome, and Dineh-Bi-Keyah Barker Creek, 235 Mya for the Navajo Springs and Pinta Dome fields, 370 Mya for the Dineh-Bi-Keyah McCracken interval, and 30 Mya for the Dineh-Bi-Keyah sill. We assume a 100% efficiency in the release (e.g., Holland et al., 2013; Warr et al., 2018), migration, and trapping of helium in the reservoirs; this generates a minimum area value to source helium.

Helium production in-situ contributes ~12% of the helium in the Ratherford Field, and for the remaining fields the contribution is <1% (Table A.12). Therefore, externally sourced helium (i.e., from sediments outside the field area or from the basement beneath the field area) must account for nearly 88% for Ratherford helium and ~ 99% for the remaining helium. Based on rock volumes beneath the field area, the factor by which the volume area is required to be increased to source 100% of its helium from in-situ production is summarized in Table A.12 (Ratherford 8×; Tocito Dome 107×; Navajo Springs 145×; Pinta Dome 116×; DBK Barker Creek 325×; DBK McCracken 700i, and DBK sill 3275×).

Based off these initial calculations concerning the helium production from within the reservoir and known field boundaries, coupled with the fact that it is geologically unlikely to achieve 100% release, migration, and trapping even in the most fortuitous scenarios (especially when considering closure temperatures and thermal gradients), leads us to conclude that in-situ reservoir helium production is insufficient to explain the observed reservoir helium occurrences.

5.5.2. External helium production

Examining helium production from external sources consists of calculating the helium generating potential of the underlying sedimentary column and the basement at specific time intervals (Tables A.13-A.15). The Precambrian time interval (540 Mya) represents the lithologic interval immediately on top of the Precambrian granitic basement and we consider it to be impermeable to significant helium escape. The timing intervals of the sedimentary reservoirs correlate to sealing horizons that are stated in section 5.5.1.

Regarding the calculation of helium generated externally, Eqs. 4 and 6 were utilized to determine the helium generated from the entire sedimentary column and basement section up to 32,808 ft (10 km) beneath the respective fields. The external flux of ^{4}He atoms is defined as:

$$^4He \text{ atoms external} = \left(q^c_{4He}\right) \times S \quad (6)$$

where q^c ^{4}He is the average external crustal ^{4}He flux (atoms) / (cm^2) = (p × α × H× (1-ϕ)), where p is the average crustal rock density 2.7 g/cm^3, α is the ^{4}He atoms grams^{-1} (Eq. 4), H is the crust thickness in cm, ϕ is the porosity, and S is the gas bearing or field area cm^2 (Buttitta et al., 2020).

As the basement porosity is largely unknown in this region, we have retained the average porosity of the reservoirs for the entire sedimentary column and have assumed an average porosity of 1% for the basement with granite as the dominant lithology (Flawn, 1956; Bickford et al., 1981; Sherwood-Lollar et al., 2014).

Regarding the mineralogy within the basement, we consider several minerals (apatite, zircon, and titanite), which are known to contain helium within their structure (Ballentine and Burnard, 2002; Danabalan, 2017; Halford, 2018; Danabalan et al., 2022). For our study we only assume: 1) the minimum threshold of helium release of 55 °C of apatite and 2) that temperatures above 55 °C will yield 100% of helium flux from minerals (Ballentine et al., 1994; Wolf et al., 1996; Ballentine and Sherwood-Lollar, 2002; Shuster et al., 2006; Reich et al., 2007; Hunt et al., 2012; Danabalan, 2017, Danabalan et al., 2022). Utilizing apatite represents a conservative approach, while other minerals would result in even higher helium estimates. Based on the reservoir temperatures in Table A.2, and an average gradient of 1.4 °F/100 ft. (~25 °C/km) (Reiter et al., 1979), the sedimentary columns and basement portions have been adjusted for the intervals that lie within the proper closure temperature interval (i.e., > 55 °C) (Table A.13). Helium amounts have not been affected for the Tocito Dome Field as it is above the closure temperature release interval for apatite. Based on the proximity to basement faults, we also assume that there are mechanisms that will allow helium flux from the basement as granitic rocks are relatively impermeable to helium (i.e., helium released remains trapped within the basement without release mechanisms).

Examining the mass balance model of ^{4}He from sedimentary external sources (reservoir + underlying sedimentary column), we observe the low helium producing Ratherford Field is the only area which can be reasonably explained by sedimentary contribution alone at a timescale of 300 Ma (which represents the assumed sealing horizon), requiring 12% of ^{4}He generation from the sediments needed to fill the reservoir volume of the field (i.e., to account for the OHIP) (Table A.14). Additionally, for the Tocito Dome, Navajo Springs, Pinta Dome, and Dineh-Bi-Keyah fields, we conclude that ^{4}He cannot be derived solely from the entire sedimentary column beneath the field outline as the potential helium producing zones are largely outside of the closure temperature interval.

Examining the mass balance model of ^{4}He from basement external sources with an assumed sealing horizon of ~540 Ma and within the proper helium release temperature interval, we observe much more realistic percentages of ^{4}He generation needed from basement required to fill the reservoir volume (to account for OHIP) for the hydrocarbon-rich fields (Ratherford: 0.3%, and Tocito Dome: 3.6%). Regarding the helium-rich fields in the proper helium release temperature window, we also calculate more reasonable percentages of ^{4}He generation needed from the basement to fill the reservoir with Navajo Springs at 5.98%, Pinta Dome at 9.38%, and the Barker Creek, McCracken and sill intervals of the Dineh-Bi-Keyah Field at 47.63%, 91.32%, and 47.05% respectively (Table A.15). It is important to note, these calculations are only for the volume of rock directly underneath the field area.

An observation from the mass balance model is that the sedimentary column cannot supply adequate volumes of helium to match OHIP calculations given shorter time scales, thus suggesting long stable intervals that could allow the helium to be generated from the basement. This basement generated helium is ultimately released due to tectonic activity (i.e., uplift of the Colorado Plateau and activation of associated basement faults/shear zones) and then subsequently migrates and is trapped in a reservoir. Therefore, the most plausible explanation suggests either an old dominant basement source with a helium flux due to tectonic activity or various episodes of extensive migration from areas several orders of magnitude larger than the fields of interest, consistent with the degree of water contact required.

6. Conclusion

Helium is a valuable economic resource, which is in increasing demand and of short supply. Here we investigate the nature of He-rich systems on the Colorado Plateau by combining bulk gas analyses and isotopic analyses of noble gases, hydrocarbons, and non-hydrocarbons. This approach allows us to classify different helium systems. Nitrogen and helium ratios indicate similar transport mechanisms and sources. Integrating δ^{15}N isotopes with noble gas isotopes and bulk nitrogen suggests a crustal origin for He and N_2 gases in He-rich samples.

Hydrocarbon-rich samples are explained by oil/water equilibrium models with air admixture. Utilizing a decoupled advective transport model, the highly unfractionated $^4He/N_2$ signatures (i.e., the crustal $^4He/N_2$ production ratio that has not been diluted by hydrocarbons) of high-helium samples are explained by primary gas migration from the basement via active tectonics. A multi-phase water gas model (open system Rayleigh fractionation), which indicates migration transport over large distances, accounts for the extremely fractionated $^{20}Ne/^{36}Ar$ values of the helium-rich samples, but does not affect $^4He/N_2$ due to water saturation with crustal gases released from the basement. Quantitative helium mass balance models examining helium production from various lithological intervals and time periods of the field area reveal that: 1) external (non-reservoir) helium sources are required, 2) long stable periods are favorable for helium accumulations, and 3) the predominant helium source in the Four Corners area is likely to be from the shallow crust (i.e., Precambrian granitic basement) utilizing a large area beneath the field (i.e., crustal gas mobilization and transport via fracture zones), consistent with the degree of water contact.

Declaration of Competing Interest

The authors declare that they have no known competing financial interests or personal relationships that could have appeared to influence the work reported in this paper.

Acknowledgements

This research has been supported in part by funding from the Division of Energy and Mineral Development, Office of Indian Energy and Economic Development, Bureau of Indian Affairs. This work has benefited greatly from discussions with Dr. Hunt, Dr. Gluyas, Dr. Flude, and Dr. Cheng. Additional thanks to Scott Sears and Tony Hines (IACX Energy); Matt Silverman, John Thomas, Billy Schneider, and Helen Trujillo (Robert L. Bayless, Producer LLC); Dave Burns and Gary Wooten (Capital Operating Group LLC); Alfred Redhouse, Donnie Trimble, Jeff Roedell, Steve Hoppe, and Steven Sandoval (Elk Petroleum Limited formerly Resolute Energy), who allowed the sampling of natural gas from various privately owned and operated oil/gas fields.

Appendix A. Supplementary data

Supplementary data to this article can be found online at https://doi.org/10.1016/j.chemgeo.2022.120790.

References

Anderson, S.T., 2018. Economics, helium, and the U.S. federal helium reserve: summary and outlook. Nat. Resour. Res. 27, 455–477. https://doi.org/10.1007/s11053-017-9359-y.

Andrews, J., 1985. The isotopic composition of radiogenic helium and its use to study groundwater movement in confined aquifers Chem. Geol. 49 (1–3), 339–351.

Aregbe, Y., Valkiers, S., Mayer, K., De Bie'vre P., 1996. Comparative isotopic measurements on xenon and krypton. Int. J. Mass Spectrom. Ion Process. 153 (1), L1–L5.

Atkins, P., De Paula, J., 2006. Atkin's Physical Chemistry. Oxford University Press, Oxford.

Baars, D.L., 2000. The Colorado Plateau: A Geologic History. University of New Mexico Press, 268 pgs.

Ballentine, C.J., Burnard, P.G., 2002. Production, release, and transport of noble gases in the continental crust. Rev. Mineral. Geochem. 47, 481–538.

Ballentine, C.J., Holland, G., 2008. What CO_2 well gases tell us about the origin of noble gases in the mantle and their relationship to the atmosphere. Phil. Trans. R. Soc. A 366, 4183–4203.

Ballentine, C.J., Mazurek, M., Gautschi, A., 1994. Thermal constraints on crustal rare gas release and migration: Evidence from Alpine fluid inclusions. Geochimica et cosmochimica acta 58 (20), 4333–4348.

Ballentine, C.J., O'Nions, R.K., 1992. The nature of mantle neon contributions to Vienna Basin hydrocarbon reservoirs. Earth Planet. Sci. Lett. 113, 553–567. https://doi.org/10.1016/0012-821X(92)90131-E.

Ballentine, C.J., O'Nions, R.K., 1994. The use of He, Ne and Ar isotopes to study hydrocarbon related fluid provenance, migration and mass balance in sedimentary basins. In: Parnell, J. (Ed.), Geofluids: Origin, Migration and Evolution of Fluids in Sedimentary Basins, Vol. 78, pp. 347–361.

Ballentine, C.J., Burgess, R., Marty, B., 2002. Tracing fluid origin, transport and interaction in the crust. In: Porcelli, D., Ballentine, C., Wieler, R. (Eds.), Noble Gases in Geochemistry and Cosmochemistry. Geochemical Society, Mineralogical Society of America, pp. 539–614.

Barry, P.H., Lawson, M., Meurer, W.P., Warr, O., Mabry, J.C., Byrne, D.J., Ballentine, C. J., 2016. Noble gases solubility models of hydrocarbon charge mechanism in the Sleipner Vest gas field. Geochim. Cosmochim. Acta 194, 291–309.

Barry, P.H., Lawson, M., Meurer, D. Danabalan, Mabry, J.C., Ballentine, C.J., 2017. Determining fluid migration and isolation times in multiphase crustal domains using noble gases. Geology 45 (9), 775–778. https://doi.org/10.1130/G38900.1.

Ballentine, C.J., Sherwood-Lollar, B., 2002. Regional groundwater focusing of nitrogen and noble gases into the Hugoton-Panhandle giant gas field, USA. Geochim. Cosmochim. Acta 66 (14), 2483–2497.

Barry, P.H., Kulongoski, J.T., Landon, M.K., Tyne, R.L., Gillespie, J.M., Stephens, M.J., Hillegonds, D.J., Byrne, D.J., Ballentine, C.J., 2018a. Tracing enhanced oil recovery signatures in casing gases using noble gases. Earth Planet. Sci. Lett. 496, 57–67. https://doi.org/10.1016/j.epsl.2018.05.028.

Barry, P.H., Lawson, M., Meurer, W., Cheng, A., Ballentine, C.J., 2018b. Noble gases in deepwater oils of the U.S. Gulf of Mexico. Geochem. Geophys. Geosyst. 19 https://doi.org/10.1029/2018GC007654.

Battino, R., Chen, C.A., Clever, H.L., Young, C.L., 1982. Solubility Data Series, Vol. 10. Nitrogen and Air. International Union of Pure and Applied Chemistry. Analytical Chemistry Division. Commission on Solubility Data. https://srdata.nist.gov/solubility/IUPAC/SDS-10/SDS-10.pdf.

Bebout, G.E., Fogel, M.L., 1992. Nitrogen-isotope compositions of metasedimentary rocks in the Catalina Schist, California: implications for metamorphic devolatilization history. Geochim. Cosmochim. Acta 56 (7), 2839–2849.

Bebout, G.E., Cooper, D.C., Bradley, A.D., Sadofsky, S.J., 1999. Nitrogen-isotope record of fluid-rock interactions in the Skiddaw Aureole and granite, English Lake District. Am. Mineral. 84 (10), 1495–1505.

Bickford, M.E., Harrower, K.L., Hoppe, W.J., Nelson, B.K., Nusbaum, R.L., Thomas, J.J., 1981. Rb-Sr and U-Pb geochronology and distribution of rock types in the Precambrian basement of Missouri and Kansas. Geol. Soc. Am. Bull. 92 (6), 323–341.

Boreham, C.J., Edwards, D.S., Poreda, R.J., Darrah, T.H., Zhu, R., Grosjean, E., Main, P., Waltenberg, K., Henson, P.A., 2018. Helium in the Australian liquefied natural gas economy. The APPEA J 2018 (58), 209–237.

Boyd, S.R., 2001. Ammonium as a biomarker in Precambrian metasediments. Precambrian Res. 108 (1), 159–173.

Brennan, S., East, J., Dennen, K., Jahediesfanjani, H., Varela, B., 2016. Helium Concentrations in United States Wells. U.S. Geological Survey.

Broadhead, R.F., Gillard, L., 2004. Helium in New Mexico: Geologic Distribution and Exploration Possibilities, Open File Report No. 483. New Mexico Bureau of Geology and Mineral Resources 1–62.

Brown, A. 2010. Formation of High Helium Gases: A Guide for Explorationists*. Search and Discovery Article #80115, 2010, Posted October 29, 2010 *Adapted from poster presentation at AAPG Convention, New Orleans, LA, April 11-14, 2010. <http://www.searchanddiscovery.com/documents/2010/80115brown/ndx_brown.pdf>.

Burwash, R.A., Cumming, G.L., 1976. Uranium and thorium in the Precambrian basement 645 of western Canada. I. Abundance and distribution. Can. J. Earth Sci. 13 (2), 284–293, 646.

Buttitta, Dario, Caracausi, Antonio, Chiaraluce, Lauro, Favara, Rocco, Morticelli, Gasparo, Maurizio & Sulli, Attilio., 2020. Continental degassing of helium in an active tectonic setting (northern Italy): the role of seismicity. Sci. Rep. 10, 162. https://doi.org/10.1038/s41598-019-55678-7.

Byrne, D.J., Barry, P.H., Lawson, M., Ballentine, C.J., 2017. A Review of Noble Gases in Conventional and Unconventional Systems. From source to seep Geochemical Appl. Hydrocarb. Syst. Geol. Soc. London Spec. Publ.

Caracausi, A., Paternoster, M., 2015. Radiogenic helium degassing and rock fracturing: a case study of the southern Apennines active tectonic region. J. Geophys. Res. Solid Earth 120, 2200–2211. https://doi.org/10.1002/2014JB011462.

Cartigny, Pierre, Marty, Bernard, 2013. Nitrogen isotopes and mantle geodynamics: the emergence of life and the atmosphere-crust-mantle connection. Elements. 9, 359–366. https://doi.org/10.2113/gselements.9.5.359.

Chan, 2013. Up in the AIR: The BLM's Disappearing Helium Program, 10. Committee on Understanding the Impact of Selling the Helium Reserve, National Research Council of the National Academies, May, p. 2012.

Clarke, W.B., Jenkins, W.J., Top, Z., 1976. Determination of tritium by mass spectrometric measurement of 3 he. Int. J. Appl. Radiat. Isot. 27 (9), 515–522.

Condie, K.C., 1986. Geochemistry and tectonic setting of early proterozoic supracrustal rocks in the Southwestern United States. J. Geol. 94 (6), 845–864.

Craddock, W.H., Blondes, M.S., DeVera, C.A., Hunt, A.G., 2017. Mantle and crustal gases of the Colorado Plateau: geochemistry, sources, and migration pathways. Geochim. Cosmochim. Acta. https://doi.org/10.1016/j.gca.2017.05.017.

Danabalan, D., 2017. Helium: Exploration Methodology for a Strategic Resource. Doctoral thesis. Durham University.

Danabalan, D., Gluyas, J., Macpherson, C., Abraham-James, T., Bluett, J., Barry, P., Ballentine, C.J., 2022. The Principles of Helium Exploration. Petroleum Geoscience 28 (2). https://doi.org/10.1144/petgeo2021-029.

Danie, T.C., 1978. Dineh-bi-Keyah (Oil), T. 35–36 N., R. 29–30 E., G&SRM Apache County, Arizona. Four Corners Geological Society. Oil and Gas Fields of the Four Corners Area, V I-II, pp. 73–76.

Darrah, T., Poreda, R.J., 2012. Evaluating the accretion of meteoritic debris and interplanetary dust particles in the GPC-3 sediment core using noble gas and

mineralogical tracers. Geochimica et Cosmochimica Acta 84, 329–352. https://doi.org/10.1016/j.gca.2012.01.030.
Darrah, T., Tedesco, D., Tassi, F., Vaselli, O., Cuoco, E., Poreda, R., 2013. Gas chemistry of the Dallol region of the Danakil Depression in the Afar region of the northern-most East African Rift. Chem. Geol. 339, 16–29.
Darrah, T., Vengosh, A.V., Jackson, R.B., Warner, N.R., Poreda, R.J., 2014. Noble gases identify the mechanism of fugitive gas contamination in drinking water wells overlying the Marcellus and Barnett shales. PNAS. 111 (39), 14076–14081.
Darrah, T., Jackson, R.B., Vengosh, A., Warner, N.R., Whyte, C.J., Walsh, T.B., Kondash, R.J., Poreda, R.J., 2015. The evolution of Devonian hydrocarbon gases in shallow aquifers of the northern Appalachian Basin: insights from integrating noble gas and hydrocarbon geochemistry. Geochim. Cosmochim. Acta 170.
Davis, G.H., Bump, A.P., 2009. Structural geologic evolution of the Colorado Plateau. In: Kay, S.M., Ramos, V.A., Dickinson, W.R. (Eds.), Backbone of the Americas: Shallow Subduction, Plateau Uplift, and Ridge and Terrane Collision: Geological Society of America Memoir 204, pp. 99–124. https://doi.org/10.1130/2009.1204(05).
Day, J.M., Barry, P.H., Hilton, D.R., Burgess, R., Pearson, D.G., Taylor, L.A., 2015. The helium flux from the continents and ubiquity of low-$^{3}He/^{4}He$ recycled crust and lithosphere. Geochim. Cosmochim. Acta 153, 116–133.
Ellis, G., 2014. Geochemistry of Natural Gases of the Anadarko Basin. https://doi.org/10.3133/ds69EE.
Faber, E., Stahl, W.J., Whiticar, M.J., 1992. Distinction of bacterial and thermogenic hydrocarbon gases. In: Vially, R. (Ed.), Bacterial Gas. Editions Technip, Paris, pp. 63–74.
Fassett, J.E., 2010. Oil and gas resources of the San Juan Basin, New Mexico and Colorado. New Mexico Geological Society 181–196.
Fitton, J.G., James, D., Leeman, W.P., 1991. Basic magmatism associated with late Cenozoic extension in the western United States: compositional variations in space and time. J. Geophys. Res. 96 https://doi.org/10.1029/91JB00372 issn: 0148-0227.
Flawn, P.T., 1956. Basement rocks of Texas and Southeast New Mexico: Bureau of Economic Geology. University of Texas Publications 5605, 261.
Flude, S., Warr, O., Magalhães, N., Bordmann, V., Fleury, J.M., Reis, H.L.S., Trindade, R. I., Hillegonds, D., Sherwood Lollar, B., Ballentine, C.J., 2019. Deep crustal source for hydrogen and helium gases in the São Francisco Basin, Minas Gerais, Brazil. *AGUFM, 2019*, EP51D-2111.
Foos, A., 1999. Geology of the Colorado Plateau. Geology Department, University of Akron, National Park Service.
Freeman, W.M., 1978. Aneth (Ratherford Unit) (Oil), T. 41 S., R. 23–24 E., SLPM, San Juan County, Utah. Four Corners Geological Society. Oil and Gas Fields of the Four Corners Area, V I-II, pp. 584–586.
Gevantman, L.H., 1992. Solubility of selected gases in water: for Lide DR (Ed.) CRC. In: Hand Book of Chemistry and Physics CRC Press Boca Raton, Florida, pp. 82–83.
Gilbert, H., Velasco, A.A., Zandt, G., 2007. Preservation of Proterozoic terrane boundaries within the Colorado Plateau and implications for its tectonic evolution. Earth Planet. Sci. Lett. 258, 237–248. https://doi.org/10.1016/j.epsl.2007.03.034.
Gilfillan, S.M.V., Ballentine, C.J., Holland, G., Sherwood Lollar, B., Stevens, S., Schoell, M., Cassidy, M., 2008. Natural CO_2 storage analogues: the noble gas geochemistry of natural CO_2 gas reservoirs from the Colorado Plateau and Rocky Mountain provinces, USA. Geochim. Cosmochim. Acta 72 (4), 1174–1198.
Gilfillan, S., Lollar, B., Holland, G., Blagburn, D., Stevens, S., Schoell, M., Cassidy, M., Ding, Z., Zhou, Z., Lacrampe-Couloume, G., Ballentine, C.J., 2009. Solubility trapping in formation water as dominant CO_2 sink in natural gas fields. Nature 458, 614–618. https://doi.org/10.1038/nature07852.
Haendel, D., Mühle, K., Nitzsche, H.M., Stiehl, G., Wand, U., 1986. Isotopic variations of the fixed nitrogen in metamorphic rocks. Geochim. Cosmochim. Acta 50 (5), 749–758.
Halford, D.T., 2018. Isotopic Analyses of Helium from Wells Located in the Four Corners Area, Southwestern, USA. Master's Thesis, Colorado School of Mines.
Harkness, J., Darrah, T., Warner, N., Whyte, C., Moore, M., Millot, R., Kloppman, W., Jackson, R., Vengosh, A., 2017. The geochemistry of naturally occurring methane and saline groundwater in an area of unconventional shale gas development. Geochim. Cosmochim. Acta 208. https://doi.org/10.1016/j.gca.2017.03.039.
Hernández-Uribe, D., Palin, R.M., 2019. Catastrophic shear-removal of subcontinental lithospheric mantle beneath the Colorado Plateau by the subducted Farallon slab. Sci. Rep. 9 (1) https://doi.org/10.1038/s41598-019-44628-y.
Holland, G., Lollar, B.S., Li, L., Lacrampe-Couloume, G., Slater, G.F., Ballentine, C.J., 2013. Deep fracture fluids isolated in the crust since the Precambrian era. Nature 497 (7449), 357–360.
Hunt, A., Darrah, T., Poreda, R., 2012. Determining the source and genetic fingerprint of natural gases using noble gas geochemistry: a northern Appalachian Basin case study. AAPG 96, 1785–1811.
Huntoon., 1974. The post-Paleozoic structural geology of the eastern Grand Canyon, Arizona. In: Breed, W.J., Roat, E.C. (Eds.), Geology of the Grand Canyon: Flagstaff, Ariz., Mus. Northern Arizona and Grand Canyon Natural History Assoc, pp. 82–115.
Jackson, R.B., Vengosh, A., Darrah, T.H., Warner, N.R., Down, A., Poreda, R.J., Osborn, S.G., Zhao, K., Karr, J.D., 2013. Increased stray gas abundance in a subset of drinking water wells near Marcellus shale gas extraction. Proc. Natl. Acad. Sci. U. S. A. 110 (28), 11250–11255.
Jenden, P.D., Newell, K.D., Kaplan, I.R., Watney, W.L., 1988. Composition and stable-isotope geochemistry of natural gases from Kansas, Midcontinent, USA. Chem. Geol. 71 (1–3), 117–147.
Kang, M., Christian, S., Celia, M. A., Mauzerall, D. L., Bill, M., Miller, A. R., Chen, Y., Conrad, M. E., Darrah, T. H. and Jackson, R. B. (2016). Identification and characterization of high methane emitting abandoned oil and gas wells. Proc. Natl. Acad. Sci. U. S. A., 113, p. 13,636-13,641.
Karlstrom, K.E., Bowring, S.A., 1988. Early Proterozoic Assembly of Tectonostratigraphic Terranes in Southwestern North America. J. Geol. 96 (5), 561–576.
Karolytė, R., Johnson, G., Györe, D., Serno, S., Flude, S., Stuart, F.M., Chivas, A.R., Boyce, A., Gilfillan, S., 2019. Tracing the migration of mantle CO_2 in gas fields and mineral water springs in south-east Australia using noble gas and stable isotopes. Geochim. Cosmochim. Acta 259, 109–128. ISSN 0016–7037. https://doi.org/10.1016/j.gca.2019.06.002.
Karolytė, R., Warr, O., Lacrampe-Couloume, G., van Heerden, E., Flude, S., Opperman, D. J., Bester, A., Lippmann-Pipke, J., Slater, G.F., Onstott, T.C., de Lange, F., Webb, S., Ballentine, C.J., Sherwood Lollar, B., 2022. The role of porosity in H_2/He production ratios in fracture fluids from the Witwatersrand Basin, South Africa. Chem. Geol. 595 https://doi.org/10.1016/j.chemgeo.2022.120788.
Kennedy, B., Truesdell, A., 1995. The Northwest Geysers high-temperature reservoir: evidence for active magmatic degassing and implications for the origin of The Geysers geothermal field. Geothermics 25, 365–387. https://doi.org/10.1016/0375-6505(96)00005-3.
Kipfer, R., Aeschbach-Hertig, W., Peeters, F., Stute, M., 2002. Noble gases in lakes and groundwaters. Rev. Mineral. Geochem. 47, 615–700.
Kreulen, R., Schuiling, R.D., 1982. N_2-CH_4-CO_2 fluids during formation of the Dôme de l'Agout, France. Geochim. Cosmochim. Acta 46 (2), 193–203.
Labidi, J., Barry, P.H., Bekaert, D.V., et al., 2020. Hydrothermal $^{15}N^{15}N$ abundances constrain the origins of mantle nitrogen. Nature 580, 367–371. https://doi.org/10.1038/s41586-020-2173-4.
Lee, J.Y., Marti, K., Severinghaus, J.P., Kawamura, K., Yoo, H.S., Lee, J.B., Kim, J.S., 2006. A redetermination of the isotopic abundances of atmospheric Ar. Geochim. Cosmochim. Acta 70 (17), 4507–4512.
Levander, A., Schmandt, B., Miller, M.S., Liu, K., Karlstrom, K.E., Crow, R.S., Lee, C.T.A., Humphreys, E.D., 2011. Continuing Colorado Plateau uplift by delamination-style convective lithospheric downwelling. Nature 472 (7344), 461–465.
Li, Y., Qin, S., Wang, Y., Holland, G., Zhou, Z., 2020. Tracing interaction between hydrocarbon and groundwater systems with isotope signatures preserved in the Anyue gas field, central Sichuan Basin, China. Geochim. Cosmochim. Acta 274, 261–285. https://doi.org/10.1016/j.gca.2020.01.039.
Lowenstern, J., Evans, W., Bergfeld, D., Hunt, A., 2014. Prodigious degassing of a billion years of accumulated radiogenic helium at Yellowstone. Nature. 506, 355–358. https://doi.org/10.1038/nature12992.
Magoon, L.B., Dow, W.G. (Eds.), 1994a. The petroleum system—from source to trap: American Association of Petroleum Geologists Memoir 60, 655 p.
Magoon, L.B., Dow, W.G., 1994b. The petroleum system. In: Magoon, L.B., Dow, W.G. (Eds.), The petroleum system—From source to trap: American Association of Petroleum Geologists Memoir, 60, pp. 3–24.
Marty, B., Zimmermann, L., Humbert, F., 1996. Nitrogen isotopic composition of the silicate Earth and its bearing on Earth-atmosphere evolution. Lunar Planet. Sci 27 (1996), 819–820.
Marty, B., Zimmermann, L., Pujol, M., Burgess, R., Philippot, P., 2013. Nitrogen Isotopic Composition and Density of the Archean Atmosphere. Science, American Association for the Advancement of Science. https://doi.org/10.1126/science.1240971.
Masters, J.A., 2000. The Slow Discovery of Dineh-Bi-Keyah. The Mountain Geologist, 37 (2), 91–100.
McKenny, K.W., Masters, J.A., 1968. Dineh-Bi-Keyah, Apache County, Arizona. AAPG Bull. 52 (10), 2045–2057.
Mingram, B., Hoth, P., Lüders, V., Harlov, D., 2005. The significance of fixed ammonium in Paleozoic sediments for the generation of nitrogen-rich natural gases in the North German Basin. Int. J. Earth Sci. 94 (5–6), 1010–1022.
Mireault, R., Dean, L., Esho, N., Kupchenko, C., Mattar, L., Morad, K., Pooladi-Darvish, M., 2007. Reservoir Engineering for Geologists. Canadian Society of Petroleum Geologists Reservoir magazine. http://large.stanford.edu/courses/2013/ph240/zaydullin2/docs/fekete.pdf.
Moreira, M., Allegre, C.J., 1998. Helium-neon systematic and the structure of the mantle. Chem. Geol. 147, 53–59.
National Research Council, 2010. Selling the Nation's Helium Reserve. The National Academies Press, Washington, DC. https://doi.org/10.17226/12844.
Ozima, M., Podosek, F.A., 2002. Noble Gas Geochemistry, 2nd. Cambridge University Press, Cambridge, New York, Melbourne, pp. xiv–286.
Pepin, R.O., 2000. On the isotopic composition of primordial xenon in terrestrial planet atmospheres. In: From Dust to Terrestrial Planets. Springer, Netherlands, pp. 371–395.
Pinti, D.L., Marty, B., 2000. Chapter 7 Noble gases in oil and gas fields: origins and processes. Mineralogical Association of Canada Short Course Vol. 28, 160–169.
Porcelli, D., Ballentine, C.J., 2002. Models for the distribution of terrestrial noble gases and the evolution of the atmosphere. Rev. Mineral. Geochem. 47, 411–480.
Prinzhofer, A., 2013. Noble gases in oil and gas accumulations. In: The Noble Gases as Geochemical Tracers. Springer, Berlin Heidelberg, pp. 225–247.
Rauzi, S.L., 2003. Review of Helium Production and Potential in Arizona. Arizona Geological Survey, Open-File Report OFR, pp. 03–05. http://repository.azgs.az.gov/sites/default/files/dlio/files/2010/u14/ofr_03_05.pdf>.
Rauzi, S.L., 2015. Dineh-Bi-Keyah Oil Field, Apache Country, Arizona. Arizona Geological Survey Publication OG-15.
Re, G., 2017. Evolution and dynamics of a monogenetic volcanic complex in the southern Hopi Buttes Volcanic Field (AZ, US): magma Diversion and Fragmentation Processes at the Jagged Rocks Complex (Thesis, Doctor of Philosophy). University of Otago. Retrieved from. http://hdl.handle.net/10523/7358.
Reich, M., Ewing, R.C., Ehlers, T.A., Becker, U., 2007. Low-temperature anisotropic diffusion of helium in zircon: implications for zircon (U–Th)/He thermochronometry. Geochim. Cosmochim. Acta 71 (12), 3119–3130.

Reiter, M., Mansure, A.J., Shearer, C., 1979. Geothermal characteristics of the Colorado Plateau. Tectonophysics 61, 183–195.
Roberts, G.G., White, N.J., Martin-Brandis, G.L., Crosby, A.G., 2012. An uplift history of the Colorado Plateau and its surroundings from inverse modeling of longitudinal river profiles. Tectonics 31, TC4022. https://doi.org/10.1029/2012TC003107.
Robinson, D.B., Peng, D.Y., 1976. A new two-constant equation of state industrial and engineering chemistry: fundamentals. Ind. Eng. Chem. Fundam. 15, 59–64. https://doi.org/10.1021/i160057a011.
Roy, M., 2005. A summary of ideas on the timing and distribution of rock and surface uplift across the Colorado Plateau: Geological Society of America Abstracts with Programs. v. 37, no. 7, p. 109.
Rutledge, J. 2010. Geologic Demonstration at the Aneth Oil Field, Paradox Basin, Utah, Southwest Regional Partnership on Carbon Sequestration Phase II, Prepared for U.S. Department of Energy's National Energy Technology Laboratory and New Mexico Institute of Mining & Technology <https://www.osti.gov/servlets/purl/1029292>.
Sano, Y., Wakita, H., Sheng, X., 1988. Atmospheric helium isotope ratio. Geochem. J. 22 (4), 177–181.
Schoell, M., 1983. Genetic characterization of natural gases. AAPG Bull. 67, 2225–2238.
Schoell, M., 1988. Multiple origins of methane in the earth. Chem. Geol. 71, 1–10.
Selley, R.C, and Sonnenberg, S. (2015). Elements of Petroleum Geology third edition. Academic Press. pgs. 526.
Sherwood-Lollar, B., Onstott, T., Lacrampe-Couloume, G., et al., 2014. The contribution of the Precambrian continental lithosphere to global H_2 production. Nature 516, 379–382. https://doi.org/10.1038/nature14017.
Shuster, D.L., Flowers, R.M., Farley, K.A., 2006. The influence of natural radiation damage on helium diffusion kinetics in apatite. Earth Planet. Sci. Lett. 249 (3), 148–161.
Sims, P.K., Saltus, R.W., Anderson, E.D., 2008. Precambrian basement structure map of the continental United States—An interpretation of geologic and aeromagnetic data: U.S. Geological Survey Scientific Investigations Map 3012, scale: 1:8,000,000.
Sorenson, R., 2005. A dynamic model for the Permian Panhandle and Hugoton fields, Western Anadarko basin. AAPG Bulletin - AAPG Bull. 89, 921–938. https://doi.org/10.1306/03010504045.
Spencer, C.W., 1978. Tocito Dome Pennsylvanian "D" (Oil), T. 26 N., R. 18 W., NMPM, San Juan County, New Mexico. Four Corners Geological Society. Oil and Gas Fields of the Four Corners Area, V I-II, pp. 522–527.
Tedesco, D., Tassi, F., Vaselli, O., Poreda, R., Darrah, T., Cuoco, E., Yalire, M.M., 2010. Gas isotopic signatures (He, C, and Ar) in the Lake Kivu region (western branch of the East African rift system): Geodynamic and volcanological implications. J. Geophys. Res. 115, B01205. https://doi.org/10.1029/2008JB006227.
Tingey, D.G., Christiansen, E.H., Best, M.G., Ruiz, J., Lux, D.R., 1991. Tertiary minette and melanephelinite dikes, Wasatch Plateau, Utah: Records of mantle heterogeneities and changing tectonics. J. Geophys. Res. 96, 13529–13544.
Tolstikhin, I., Tarakanov, S., Gannibal, M., Waber, H.N., 2010. Production, migration, redistribution and loss of helium isotopes in sedimentary rocks. Geophys. Res. Abstr. 12. EGU2010-5738. EGU General Assembly.
Torgersen, T., 2010. Continental degassing flux of ^{4}He and its variability. Geochemistry, 933 Geophysics. Geosystems 11. https://doi.org/10.1029/2009GC002930.
Travers, P., Cumella, S., Dolan, M., 2014. Using Production Gas Carbon and Hydrogen Stable Isotope Signatures to Predict Fluid Quality: Wattenberg Field Colorado USA., p. 1. https://doi.org/10.2118/169487-MS.
Trexler, C., 2014. Tectonic and Landscape Evolution of the Colorado Plateau. Eco-geomorphology report, UC Davis.
USGS, 2000-2021. Helium statistics and information. United States Geologic Survey, April, 10, 2016. http://minerals.er.usgs.gov/minerals/pubs/commodity/helium/>.
Valderrama, J., Campusano, R., Forero, L., 2016. A new generalized henry- setschenow equation for predicting the solubility of air gases (oxygen, nitrogen and argon) in seawater and saline solutions. J. Mol. Liq. 222 https://doi.org/10.1016/j.molliq.2016.07.110.
Warr, O., Sherwood Lollar, B., Fellowes, J., Sutcliffe, C.N., McDermott, J.M., Holland, G., Mabry, J.C., Ballentine, C.J., 2018. Tracing ancient hydrogeological fracture network age and compartmentalization using noble gases. Geochim. Cosmochim. Acta 222, 340–362. ISSN 0016-7037. https://doi.org/10.1016/j.gca.2017.10.022.
White, W.M., 2015. Isotope Geochemistry, Noble Gas Geochemistry. Chapter 12. Wiley-Blackwell. Textbook, Chichester.
Whiticar, M.J., Faber, E., Whelan, J.K., Simoneit, B.R.T., 1994. Thermogenic and bacterial hydrocarbon gases (free and sorbed) in Middle Valley, Juan De Fuca Ridge, leg 139. Proceedings of the Ocean Drilling Program. Sci. Res. 139, 467–477.
Williams, L.B., Ferrell, R.E., Hutcheon, I., Bakel, A.J., Walsh, M.M., Krouse, H.R., 1995. Nitrogen isotope geochemistry of organic matter and minerals during diagenesis and hydrocarbon migration. Geochim. Cosmochim. Acta 59 (4), 765–779.
Wolf, R.A., Farley, K.A., Silver, L.T., 1996. Helium diffusion and low-temperature thermochronometry of apatite. Geochim. Cosmochim. Acta 60 (21), 4231–4240.
Zhang, W., Li, Y., Zhao, F., Han, W., Li, Y., Wang, Y., Holland, G., Zhou, Z., 2019. Using noble gases to trace groundwater evolution and assess helium accumulation in Weihe Basin, central China. Geochim. Cosmochim. Acta 251, 229–246 (ISSN 0016-7037).
Zhou, Z., Ballentine, C.J., 2006. ^{4}He dating of groundwater associated with hydrocarbon reservoirs. Chem. Geol. 226, 309–327. https://doi.org/10.1016/j.chemgeo.2005.09.030.
Zhou, Z., Ballentine, C.J., Schoell, M., Stevens, S., 2012. Identifying and quantifying natural CO_2 sequestration processes over geological timescales: The Jackson Dome CO_2 Deposit, USA. Geochim. Cosmochim. Acta 86, 257–275. https://doi.org/10.1016/j.gca.2012.02.028.
Zhu, Y., Shi, B., Fang, C., 2000. The isotopic compositions of molecular nitrogen: implications on their origins in natural gas accumulations. Chem. Geol. 164 (3), 321–330.